

Interplay of topological phases in magnetic adatom-chains on top of a Rashba superconducting surface

Andreas Heimes,* Daniel Mendler, and Panagiotis Kotetes

*Institut für Theoretische Festkörperphysik and DFG-Center for Functional Nanostructures (CFN),
Karlsruhe Institute of Technology, 76128 Karlsruhe, Germany*

We investigate the topological properties and the accessible Majorana fermion (MF) phases arising in a hybrid device consisting of a chain of magnetic adatoms placed on the surface of a conventional superconductor with Rashba spin-orbit coupling (SOC). By identifying the favored classical magnetic ground state of the adatom chain, we extract the corresponding phase diagram which exhibits an interplay of ferromagnetic (FM), antiferromagnetic (AFM) and spiral orders. We determine the parameter regime for which the FM or AFM phases dominate over the spiral and additionally become stable against thermal and quantum fluctuations. For the topological analysis we focus on the FM and AFM cases and employ a low-energy effective model relying on Shiba bound states. We find that for both magnetic patterns the hybrid system behaves as a topological superconductor which can harbor one or even two MFs per edge, due to chiral symmetry. As we show, the two magnetic orderings lead to qualitatively and quantitatively distinct topological features that are reflected in the spatial profile of the MF wavefunctions. Finally, we propose directions on how to experimentally access the diverse MF phases by varying the adatom spacing, the SOC strength, or the magnetic moment of the adatoms in consideration.

PACS numbers: 74.78.-w, 74.45.+c, 75.75.-c

Materials with Rashba spin-orbit coupling (SOC) have recently attracted renewed attention due to their pivotal role for realizing artificial topological superconductors (TSCs) which harbor Majorana fermions (MFs) [1–5]. Early proposals involved materials with SOC, such as topological insulators [6], non-centrosymmetric SCs [7], and Rashba semiconductors [8–11], which stimulated significant experimental progress. Remarkably, a number of promising but yet not fully conclusive MF-signatures have been already reported in semiconductor-based heterostructures [12–15]. The unsettled witnessing of MFs [16–18] constitutes a strong motivation for engineering and testing alternative hybrid devices. For instance, platforms based on magnetic adatoms which can be manipulated and probed via spin-polarized and spatially-resolved scanning tunneling microscopy (STM) techniques, appear capable of unambiguously revealing the presence of MFs.

This new perspective opened the door for new MF devices based on magnetic adatoms on the surface of conventional superconductors. One finds implementations with magnetic adatoms where the ordering is random [19], spiral [20–29], antiferromagnetic (AFM) with SOC induced by the combination of Zeeman fields and supercurrents [30], and ferromagnetic (FM) on top of a superconducting surface with Rashba SOC [31, 32]. According to very recent experimental findings [33], MFs seem to indeed emerge in magnetic adatom hybrid devices, where the ordering of the chain appears to be ferromagnetic. This type of ordering can lead to MFs only if Rashba SOC is present, arising from the broken inversion asso-

ciated with the Pb superconducting substrate. In fact, this is a plausible scenario for Pb which owes already a non-negligible intrinsic SOC [34]. Evenmore, it has been shown that the Rashba SOC arising in Pb quantum well structures can be considerably large and tunable [35–38]. The related SOC strength can even reach a corresponding momentum splitting of the order of $\delta k \sim 0.05 k_F$, where k_F is the Fermi-momentum ($\hbar = 1$).

In this work we focus on a platform directly related to the recent experiment of Ref. [33]. Specifically we consider a single chain consisting of classical magnetic adatoms deposited on top of the surface of a SC with Rashba SOC. We first infer the energetically favored classical magnetic order of the chain, out of the possible FM, AFM and spiral profiles. Secondly, we investigate the topological properties of the arising engineered TSCs, particularly focusing on the topological FM and AFM chains.

In the first part of the manuscript, we explore the competition of the three aforementioned magnetic profiles by assuming identical adatoms owing a fixed spin S . The magnetic atoms interact via a Ruderman-Kittel-Kasuya-Yosida (RKKY)-type superexchange [39], which is mediated by the electrons of the SC. Due to the presence of SOC, the resulting superexchange interaction is anisotropic and includes a Dzyaloshinsky-Moriya (DM) contribution [40]. The latter favors spiral ordering which is stable against disorder if the SOC is sufficiently large [41]. On the other hand, FM and AFM orders are stabilized by Ising-type anisotropy terms, induced by the crystal field of the substrate, which favor an easy axis for the magnetic ordering (see Fig. 1). By taking into account the various interactions, we extract the resulting magnetic phase diagram by additionally varying the distance of the adatoms. In this manner, our results address

*Electronic address: andreas.heimes@kit.edu

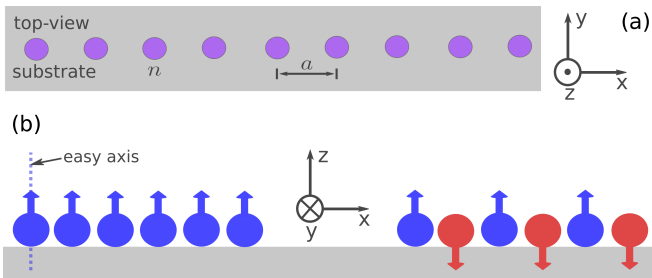


Figure 1: (a) Top view of a chain of adatoms placed on top of a superconducting surface with Rashba spin-orbit coupling (SOC). In the *absence* of magnetism, the point group symmetry of the hybrid structure, is C_{2v} , consisting of two reflection operations σ_{xz} and σ_{yz} (the index shows the mirror plane), and a C_2 rotation $(x, y, z) \rightarrow (-x, -y, z)$. (b) Side view of the hybrid structure. Crystal field effects (CFEs) violate spin rotational symmetry and favor an easy spin axis for the magnetic ordering (here z axis). On the other hand, SOC induces a Dzyaloshinsky-Moriya (DM) interaction. When the spin anisotropy dominates over the DM interaction, the adatoms order in a ferromagnetic (FM) or antiferromagnetic (AFM) fashion, depending on the chain constant a . Otherwise, the spiral (SP) ordering prevails.

implementations with alternative substrates, either due to a different superconducting material or orientation of the surface involved.

In the second part, we focus on the topological properties of these platforms, and concentrate on the FM and AFM cases. This is justified, as the findings of Ref. [33] indicate a strong Ising anisotropy, which as we show here, can additionally render the FM and AFM phases inert to quantum and thermal fluctuations in spite of the one-dimensional character of the chain. For extracting the topological phase diagram, we first retrieve an effective low-energy model based on Shiba states [42], which constitute midgap electronic states of the SC localized at the sites of the adatoms. The symmetry properties of the system gives rise to a rich phase diagram of MF-phases with 0, 1, or 2 MFs per chain edge. One can access the three phases via varying the adatom distance, the strength of the SOC and the value of the magnetic moment. The phases with 2 MFs per chain edge are topologically protected by chiral [32, 43–46] symmetry, and they indeed become accessible here for the parameters adopted. For illustrating the relevant mechanism driving the diverse topological phases, we identify the relevant gap closings in the Shiba bandstructure, which provide insight for manipulating the MFs and tailoring the topological properties of these platforms.

Our paper is structured as follows: In Sec. I we obtain the magnetic phase diagram for a magnetic chain on top of a metallic surface with Rashba SOC. We consider that the magnetic adatoms interact via an RKKY interaction, while at the same time they experience a crystal field induced Ising anisotropy. In Sec. II we extend the previous analysis for the case of a superconducting substrate and

discuss the modifications on the interplay of the spiral, FM and AFM phases. In Sec. III, we retrieve an effective one-dimensional low-energy Hamiltonian of the hybrid device for the FM and AFM implementations, relying on Shiba bound states. In Secs. IV and V, we extract the topological phase diagrams and study the arising MF wavefunction characteristics, for the FM and AFM Shiba chains, respectively. Finally, we present our conclusions in Sec. VI.

I. MAGNETIC PHASES OF AN ADATOM CHAIN ON A RASHBA METALLIC SURFACE

In this section we discuss the favored ordering of a chain of magnetic atoms placed on top of a metallic surface with Rashba SOC. We first retrieve the RKKY superexchange interaction between the magnetic atoms, which is mediated by the substrate electrons. By additionally taking into account an Ising-like anisotropy term due to the crystal field, we retrieve the classical magnetic phase diagram, which consists of FM, AFM and spiral phases. Finally, we investigate the impact of quantum and thermal fluctuations on the FM and AFM magnetic orders, and show that they are stable.

A. RKKY interaction

We start with the Hamiltonian of a two dimensional metallic substrate with Rashba SOC:

$$H_{\text{metal}} = \sum_{\mathbf{k}} \psi_{\mathbf{k}}^{\dagger} h_{\mathbf{k}} \psi_{\mathbf{k}}, \quad (1)$$

where $h_{\mathbf{k}} = \xi_{\mathbf{k}} + \alpha(\mathbf{k} \times \hat{z}) \cdot \boldsymbol{\sigma}$ is a 2×2 matrix in spin-space and $\psi_{\mathbf{k}}^{\dagger} = (c_{\mathbf{k}\uparrow}^{\dagger}, c_{\mathbf{k}\downarrow}^{\dagger})$ is the corresponding spinor. Furthermore, $c_{\mathbf{k}\sigma}^{\dagger}$ creates an electron with momentum \mathbf{k} and spin projection σ . The quadratic electronic dispersion, $\xi_{\mathbf{k}} = k^2/2m - \mu$, can be linearized around the Fermi-momentum ($k_F = \sqrt{2m\mu}$), i.e. $\xi_{\mathbf{k}} = v_F(k - k_F)$, where $k = |\mathbf{k}|$ and v_F is the Fermi-velocity. The Hamiltonian $h_{\mathbf{k}}$ can be readily diagonalized via a $\pi/2$ -rotation about the $\hat{\mathbf{k}}$ -axis:

$$e^{i\frac{\pi}{4}\hat{\mathbf{k}} \cdot \boldsymbol{\sigma}} h_{\mathbf{k}} e^{-i\frac{\pi}{4}\hat{\mathbf{k}} \cdot \boldsymbol{\sigma}} = \xi_{\mathbf{k}} + \alpha k \sigma_z, \quad (2)$$

where $\hat{\mathbf{k}} = \mathbf{k}/k$. The respective eigenenergies are given by $\xi_{k\lambda} = \xi_{\mathbf{k}} + \lambda \alpha k \approx v_F(k - k_{\lambda})$, with $k_{\lambda} \approx k_F(1 - \alpha\lambda/v_F)$, corresponding to the two helicity bands $\lambda = \pm 1$. Thus, the effective momentum splitting δk corresponds to a SOC strength $\alpha = v_F \delta k/k_F$.

In order to proceed, we define the Matsubara Green's function in the helicity subspace: $g_{\lambda}(k, i\omega) = (i\omega - \xi_{k\lambda})^{-1}$ and with that we obtain

$$(i\omega - \xi_{\mathbf{k}} - \alpha k \sigma_z)^{-1} = \sum_{\lambda=\pm} \frac{1 + \lambda \sigma_z}{2} g_{\lambda}(k, i\omega). \quad (3)$$

According to the result above, the electronic Green's function is given by

$$\begin{aligned} G(\mathbf{k}, i\omega) &= \sum_{\lambda=\pm} \frac{1 + \lambda e^{-i\frac{\pi}{4}\hat{\mathbf{k}}\cdot\boldsymbol{\sigma}} \sigma_z e^{i\frac{\pi}{4}\hat{\mathbf{k}}\cdot\boldsymbol{\sigma}}}{2} g_{\lambda}(k, i\omega) \\ &= \sum_{\lambda=\pm} \frac{1 + \lambda(\hat{\mathbf{k}} \times \hat{\mathbf{z}}) \cdot \boldsymbol{\sigma}}{2} g_{\lambda}(k, i\omega). \end{aligned} \quad (4)$$

At this point, we assume a certain arrangement for the magnetic adatoms on the metallic substrate. Here we consider classical spins \mathbf{S}_i with magnitude $|\mathbf{S}_i| = S$, placed at positions $\mathbf{R}_i = ia\hat{\mathbf{x}}$, with $i = 1, \dots, N$. In addition, we consider that the interaction between the adatoms is driven by an exchange interaction mediated by the conduction electrons of the substrate. The coupling between adatoms and conduction electrons can be parametrized by an exchange energy J , i.e.

$$H_J = J \sum_{i=1}^N \iint \frac{d\mathbf{k}d\mathbf{k}'}{(2\pi)^2} e^{-i(\mathbf{k}-\mathbf{k}')\cdot\mathbf{R}_i} c_{\mathbf{k}\sigma}^{\dagger} (\mathbf{S}_i \cdot \boldsymbol{\sigma})_{\sigma\sigma'} c_{\mathbf{k}'\sigma'}. \quad (5)$$

Given that J is a small coupling constant and that the local modifications of the electronic spectrum in the substrate are negligible, we can follow a standard one-loop expansion and obtain an effective spin-spin interaction. The so called RKKY interaction reads [39]

$$H_{\text{RKKY}} = -\frac{J^2}{2} \sum_{ij} \chi_{ij}^{\alpha\beta} S_i^{\alpha} S_j^{\beta}, \quad (6)$$

where the spin susceptibility can be derived using the Green's function given in Eq. (4):

$$\chi_{ij}^{\alpha\beta} = -T \sum_{\omega} \text{Tr}_{\sigma} [\sigma^{\alpha} G(\mathbf{R}_i - \mathbf{R}_j, i\omega) \sigma^{\beta} G(\mathbf{R}_j - \mathbf{R}_i, i\omega)], \quad (7)$$

where $G(\mathbf{R}, i\omega) = \int \frac{d\mathbf{k}}{(2\pi)^2} e^{i\mathbf{k}\cdot\mathbf{R}} G(\mathbf{k}, i\omega)$. In the following we will consider a chain of adatoms with magnetic moments placed along the x direction. In Appendix A we present in detail the steps which yield the well known result [47] for the RKKY interaction:

$$\begin{aligned} H_{\text{RKKY}} &= -m \left(\frac{Jk_F}{\pi} \right)^2 \sum_{ij} \frac{\sin(2k_F|r_{ij}|)}{(2k_F r_{ij})^2} \\ &\times \left\{ \cos(2mar_{ij}) \mathbf{S}_i \cdot \mathbf{S}_j + [1 - \cos(2mar_{ij})] S_i^y S_j^y \right. \\ &\quad \left. + \sin(2mar_{ij}) (\mathbf{S}_i \times \mathbf{S}_j)_y \right\}, \end{aligned} \quad (8)$$

where $\nu_F = m/2\pi$ is the density of states at the Fermi-level for each spin-band and $r_{ij} \equiv (i-j)a$. Eq. (8) holds in the limit $k_F a \gg 1$. For vanishing SOC, we recover the usual spin rotationally invariant Heisenberg interaction, proportional to $\mathbf{S}_i \cdot \mathbf{S}_j$. On the other hand, a finite SOC

produces both an additional Ising interaction $S_i^y S_j^y$ and a DM interaction $(\mathbf{S}_i \times \mathbf{S}_j)_y$. Note, that the particular form for the RKKY interaction could have been readily retrieved by considering all the bilinear spin-spin interaction terms, which are allowed by the C_{2v} point group symmetry of the system in the non-magnetic phase.

We may write the RKKY interaction in a compact fashion, by taking into account that the rotation of a classical spin \mathbf{S}_j by an angle $\theta_{ij} = 2mar_{ij}$ with respect to \mathbf{S}_i , is given by

$$\mathbf{S}_j(\theta_{ij}) \equiv \cos(\theta_{ij}) \mathbf{S}_j + \sin(\theta_{ij}) (\hat{\mathbf{y}} \times \mathbf{S}_j). \quad (9)$$

Thus we may rewrite Eq. (8) as follows [47]:

$$H_{\text{RKKY}} = -m \left(\frac{Jk_F}{\pi} \right)^2 \sum_{ij} \frac{\sin(2k_F|r_{ij}|)}{(2k_F r_{ij})^2} \mathbf{S}_i \cdot \mathbf{S}_j(\theta_{ij}). \quad (10)$$

This implies that the SOC would generally establish a spiral configuration, with a tilting angle $\theta_{i+1,i} = 2ma\alpha$ between successive spins. However, the substrate crystal field effects (CFEs), violate spin rotational invariance so that the magnetic moment of adatoms tends to point along the axis perpendicular to the surface (z axis here). This anisotropy gives rise to an additional term appearing in the total adatom Hamiltonian, which depends on the microscopic details of the substrate and can generally assume a rather complicated form. However, here we will consider the simplest allowed term with the form

$$H_{\text{CFE}} = -\frac{D}{2} \sum_i (S_i^z)^2, \quad (11)$$

which accounts for the broken spin-rotational invariance. The parameter D has been already estimated experimentally for some cases, by means of spin-polarized STM [48, 49].

B. Classical magnetic ground state

In this paragraph, we discuss the competition of the possible magnetic phases of the adatom chain (see Fig. 2), arising from the interplay of the SOC and the CFEs. The former favors a spiral ordering while the latter, if large enough, can stabilize a FM or AFM ordering depending on the adatom spacing. For the rest, we treat the spins classically, thus assuming that $|\mathbf{S}_i| = S$ with a fixed magnitude S . In the classical limit: $S \rightarrow \infty$ whereas $J \rightarrow 0$, so that JS remains finite. Later we will discuss the stability of the classical ground state against quantum and thermal fluctuations.

There are various ways to determine the classical ground state of the Hamiltonian $H_{\text{classical}} = H_{\text{CFE}} + H_{\text{RKKY}}$. In this section we pursue a rather qualitative discussion and we prefer to apply a trial configuration $\mathbf{S}_i(\vartheta) = S \sin(\vartheta) \hat{\mathbf{x}} + S \cos(\vartheta) \hat{\mathbf{z}}$, with the orientation of the spins confined in the xz plane. The latter form is

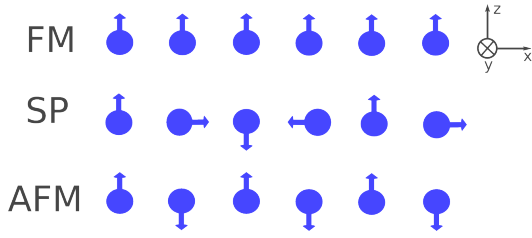


Figure 2: Possible scenarios for the classical magnetic ground state: ferromagnetic (FM), spiral (SP) and antiferromagnetic (AFM) ordering.

fixed due to **i.** the CFEs which energetically favor the appearance of finite magnetization along the easy z axis and **ii.** the mixing of the x and z magnetization components induced by the DM interaction as an indirect result of the Rashba SOC. Therefore, the particular form of the Hamiltonian implies that in the magnetic ground state, the spins are lying in the xz plane. Under these conditions, the ground state is defined by the optimal value of the angle ϑ , which minimizes the classical Hamiltonian:

$$H_{\text{classical}}(\vartheta) = -\frac{DS^2}{2} \sum_i \cos^2(\vartheta_i) \quad (12)$$

$$-m \left(\frac{JSk_F}{\pi} \right)^2 \sum_{ij} \frac{\sin(2k_F|r_{ij}|)}{(2k_F r_{ij})^2} \cos[(2m\alpha + \vartheta/a)r_{ij}].$$

We minimize this Hamiltonian with respect to ϑ for an

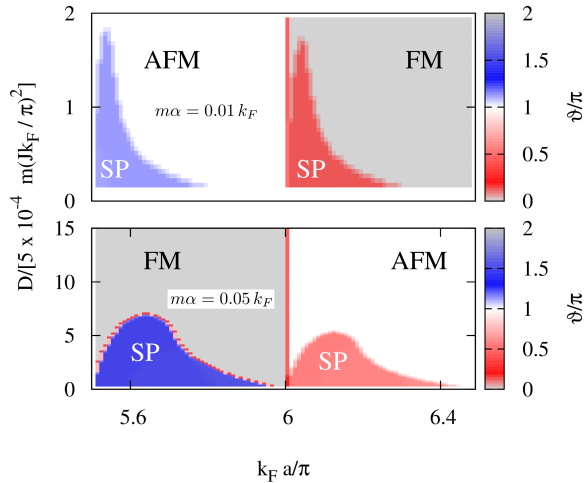


Figure 3: Phase diagrams for the classical magnetic ground state. The parameter plane is defined by the adatom spacing a , and the rescaled strength D of the crystal field anisotropy. The presented diagrams were calculated for two values of the Rashba SOC strength α . We find that large α coupling favors the spiral configuration, whereas increasing the Ising anisotropy strength D pins an easy axis (z) and promotes the FM and AFM phases.

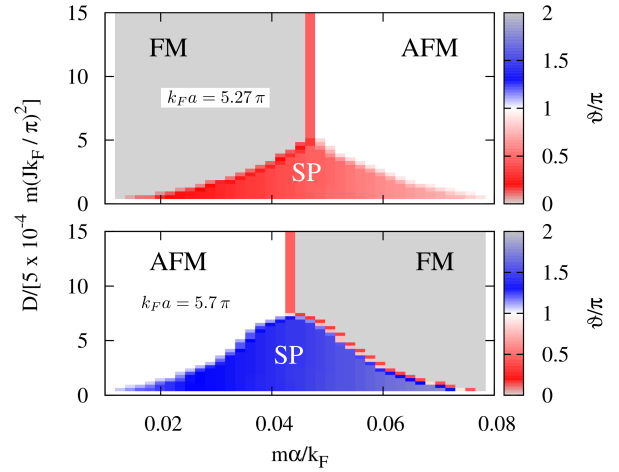


Figure 4: Phase diagrams for the classical magnetic ground state. The parameter plane is defined by the rescaled SOC strength α , and the rescaled strength D of the crystal field anisotropy. The presented diagrams were calculated for two values of the adatom spacing a . We observe stabilization of the FM or AFM phases for increasing CF anisotropy. More importantly, tuning the SOC strength can *tailor* the phase diagram leading to controllable switching between the FM and AFM phases.

infinite chain. In Fig. 3 we see that depending on the relation between: **i.** exchange energy JS , **ii.** CF anisotropy D , **iii.** SOC strength αk_F , and **iv.** adatom spacing a , the classical ground state can assume a FM ($\vartheta = 0$), AFM ($\vartheta = \pi$) or spiral configuration ($\vartheta \neq 0, \pi$). The stronger the SOC, the stronger the CF anisotropy that has to be present, in order to compensate the tendency of the system to form a spiral. Moreover, we observe that by tuning the SOC strength, as for instance by applying an electric field along the z axis, we can realize a FM \leftrightarrow AFM quantum phase transition. This can be clearly seen in Fig. 4 where the different phases are shown for two different values of the atomic spacing. The particular characteristic of the phase diagram implies that electric fields can be also employed for altering the topological properties of the Shiba chains yielding a rich landscape of MF phases. Finally, note that the arising phase transitions are first order.

C. Thermal and quantum fluctuations

In this paragraph we will investigate the robustness of the FM and AFM phases against thermal and quantum fluctuations. To this end we assume that the system resides either in the FM or the AFM phase, with $\vartheta_{\pm} = 0, \pi$ respectively. We will retrieve the dispersion of the magnetic fluctuations for each magnetic phase, by employing a Holstein-Primakoff (HP) transformation [50]. In the

limit of large S , the HP transformation reads

$$\begin{aligned} S_j^x &= (\pm 1)^j \sqrt{S/2} (b_j^\dagger + b_j), & S_j^y &= i\sqrt{S/2} (b_j^\dagger - b_j), \\ S_j^z &= (\pm 1)^j (S - b_j^\dagger b_j), \end{aligned} \quad (13)$$

with b_i and b_i^\dagger constituting bosonic operators which obey the commutation relation $[b_i, b_j^\dagger] = \delta_{ij}$, where the indices i, j refer to the sites of the adatoms. In addition, \pm corresponds to the FM (+) and the AFM (-) cases. At this point, we effect this transformation on Eq. (8) and separate the resulting quantum Hamiltonian in orders $H_{\text{quantum}}^{(m)}$ with respect to the operators b_i and b_i^\dagger . The zeroth order of the quantum Hamiltonian coincides with the classical ground state energy given by

$$H_{\text{quantum}, \pm}^{(0)} \equiv H_{\text{classical}, \pm} = -\frac{ND S^2}{2} - \sum_{ij} \Xi_{i-j}^{\pm, \alpha} S^2, \quad (14)$$

$$\Xi_{i-j}^{\pm, \alpha} \equiv (\pm 1)^{i-j} m \left(\frac{Jk_F}{\pi} \right)^2 \frac{\sin(2k_F |r_{ij}|)}{(2k_F r_{ij})^2} \cos(2m\alpha r_{ij}). \quad (15)$$

The linear term $H_{\text{quantum}}^{(1)}$ vanishes, whereas the bilinear term is given by

$$\begin{aligned} H_{\text{quantum}, \pm}^{(2)} &= -\frac{S}{2} \sum_{ij} (\Xi_{i-j}^{\pm, \alpha} - \Xi_{i-j}^{+, 0}) (b_i^\dagger b_j^\dagger + b_i b_j) \\ &\quad - \frac{S}{2} \sum_{ij} (\Xi_{i-j}^{\pm, \alpha} + \Xi_{i-j}^{+, 0}) (b_i^\dagger b_j + b_j^\dagger b_i) \\ &\quad + S \sum_{ij} \Xi_{i-j}^{\pm, \alpha} (b_i^\dagger b_i + b_j^\dagger b_j) + \frac{D}{2} (2S - 1) \sum_i b_i^\dagger b_i. \end{aligned} \quad (16)$$

In momentum space the Hamiltonian reads

$$\begin{aligned} H_{\text{quantum}, \pm}^{(2)} &= \sum_q \left[\gamma_q^{(1)} (b_q^\dagger b_q + b_{-q}^\dagger b_{-q}) \right. \\ &\quad \left. + \gamma_q^{(2)} (b_q^\dagger b_{-q}^\dagger + b_q b_{-q}) \right], \end{aligned} \quad (17)$$

with the combinations

$$\begin{aligned} \gamma_q^{(1)} &= -\frac{S}{2} (\Xi_q^{\pm, \alpha} + \Xi_q^{+, 0}) + \frac{D}{4} (2S - 1) + S \Xi_{q=0}^{\pm, \alpha} \\ \gamma_q^{(2)} &= -\frac{S}{2} (\Xi_q^{\pm, \alpha} - \Xi_q^{+, 0}) \end{aligned}$$

and $\Xi_q^{\alpha, \pm} = \sum_j \exp(iqj) \Xi_j^{\alpha, \pm}$. A bosonic Bogoliubov transformation $b_q = u_q \beta_q - v_q \beta_{-q}^\dagger$ with $u_q = \cosh \eta_q$, $v_q = \sinh \eta_q$ and $\tanh(2\eta_q) = \gamma_q^{(2)}/\gamma_q^{(1)}$, immediately provides the eigenenergies of the spin wave modes,

$$\omega_q = \sqrt{[\gamma_q^{(1)}]^2 - [\gamma_q^{(2)}]^2}.$$

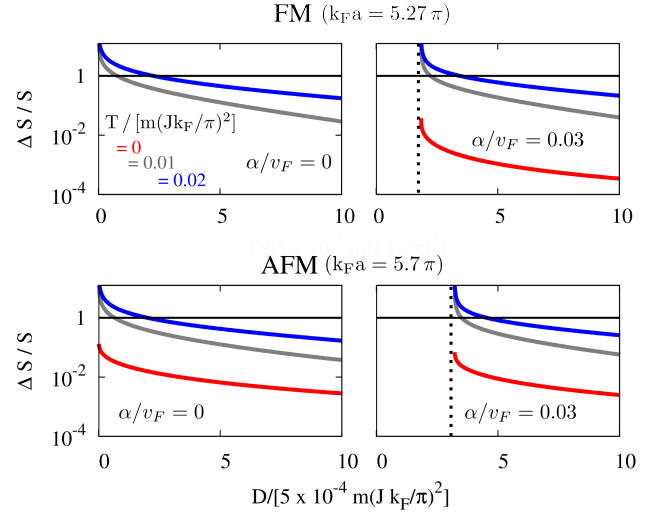


Figure 5: Sublattice-magnetization measured from its ground-state value, ΔS ($S = 15/2$), as a function of anisotropy D for different temperatures T and SOC strength α for both the AFM and the FM configuration. Both phases become unstable for $D \rightarrow 0$, since fluctuations become significant. The AFM phase always exhibits both thermal and quantum fluctuations. In contrast, quantum fluctuations appear in the FM case only when SOC is present. In both phases a sufficiently large, but experimentally feasible, value for D suppresses both types of fluctuations.

In order to investigate the stability of the FM and AFM phases, we calculate the sublattice magnetization, i.e.

$$M = -\frac{1}{N} \sum_{j=1}^N (\pm 1)^j \langle S_j^z \rangle = S - \frac{1}{N} \sum_q \langle b_q^\dagger b_q \rangle.$$

Using the Bogoliubov operators and by introducing the Bose-Einstein distribution $n_q = \langle \beta_q^\dagger \beta_q \rangle$, we obtain the deviation of the sublattice magnetization from its ground-state value

$$\Delta S = S - M = \frac{1}{N} \sum_q [n_q u_q^2 + (1+n_q) v_q^2], \quad (18)$$

where we have assumed that $\text{sgn}(\langle S_1^z \rangle) = 1$. In Fig. 5 we show ΔS for different temperatures and SOC strength. For the atomic spin we use $S = 15/2$ that has been realized in clusters of few magnetic atoms [51]. We find that for $T = 0$ and $\alpha = 0$ only the AFM configuration exhibits quantum fluctuations, which are absent in the FM case ($\Delta S = 0$). In both cases we find that quantum as well as thermal fluctuations are suppressed with increasing anisotropy D . For both AFM and FM configurations, the sum in Eq. (18) diverges for finite temperatures when taking the limit $D \rightarrow 0$, and thus thermal fluctuations destroy the magnetic order. In STM experiments the nearest neighbor exchange energy as well as the crystal field anisotropy can be measured. The next

neighbor RKKY interaction of various metals is of the order [48, 49]

$$\tilde{J} \equiv m \left(\frac{JSk_F}{\pi} \right)^2 \frac{\sin(2k_F a)}{(2k_F a)^2} \sim 0.1 \text{ meV}. \quad (19)$$

The crystal field anisotropy D has been determined in Ref. [49] to be approximately given by ~ 1 meV or even larger [48]. In terms of the parameters \tilde{J} and D our calculation covers the parameter regime $D/\tilde{J} \lesssim 10$, which is consistent with the aforementioned experimental realization. Furthermore, the so far explored temperatures are within the range $T \sim 0 - 1$ K, which are typical for the MF experiments. As a conclusion, FM or AFM magnetic chains may be established, even in the presence of strong SOC without being destroyed by fluctuations.

II. MAGNETIC PHASES OF AN ADATOM CHAIN ON A RASHBA SUPERCONDUCTOR

Here we extend the previous analysis in order to investigate the effect of superconductivity on the magnetic phase diagram. Once again, the magnetic adatoms interact via an RKKY interaction which is mediated by the electrons of the substrate superconductor, while they also feel a spin anisotropy due to the crystal field.

A. Gor'kov-Nambu Green's function

In this section we derive the Green's function for the superconducting substrate degrees of freedom in the presence of SOC. As before, we exclusively discuss Rashba SOC, although other couplings between spin and momentum may be intrinsically present. This type of SOC can be engineered and can be considerably large for instance in quantum wells [35–38]. In fact, superconducting thin films of Pb feature both intrinsic and Rashba types of SOC. Starting from the Hamiltonian of Eq. (1) for a two-dimensional metallic surface with SOC, we consider here an additional spin singlet s-wave pairing term Δ (here real and positive)

$$\begin{aligned} H_{sc} &= \frac{1}{2} \sum_{\mathbf{k}} \psi_{\mathbf{k}}^\dagger [\xi_k \tau_z + \alpha \tau_z (\hat{\mathbf{k}} \times \hat{\mathbf{z}}) \cdot \tilde{\boldsymbol{\sigma}} - \Delta \tau_y \sigma_y] \psi_{\mathbf{k}} \\ &= \frac{1}{2} \sum_{\mathbf{k}} \psi_{\mathbf{k}}^\dagger h_{\mathbf{k}} \psi_{\mathbf{k}}, \end{aligned} \quad (20)$$

where the Pauli matrices $\boldsymbol{\tau}$ are defined in particle-hole space and $\psi_{\mathbf{k}}^\dagger = (c_{\mathbf{k}\uparrow}^\dagger, c_{\mathbf{k}\downarrow}^\dagger, c_{-\mathbf{k}\uparrow}, c_{-\mathbf{k}\downarrow})$ is the corresponding spinor. Following the procedure of Sec. IA we perform a rotation, i.e.

$$e^{i\frac{\pi}{4} \hat{\mathbf{k}} \cdot \tilde{\boldsymbol{\sigma}}} h_{\mathbf{k}} e^{-i\frac{\pi}{4} \hat{\mathbf{k}} \cdot \tilde{\boldsymbol{\sigma}}} = \xi_k \tau_z + \alpha k \sigma_z - \Delta \tau_y \sigma_y.$$

Mind that the representation of the spin operator in the extended space is given by $\tilde{\boldsymbol{\sigma}}/2 = (\tau_z \sigma_x, \sigma_y, \tau_z \sigma_z)/2$. By

introducing

$$\tilde{g}_\pm(k, i\omega) = [(i\omega)^2 - \Delta^2 - \xi_{k\pm}^2]^{-1}, \quad (21)$$

we obtain

$$\begin{aligned} & [i\omega - \xi_k \tau_z - \alpha k \sigma_z + \Delta \tau_y \sigma_y]^{-1} \\ &= \sum_{\lambda=\pm} \frac{1 + \lambda \tau_z \sigma_z}{2} (i\omega + \xi_k \tau_z + \alpha k \sigma_z - \Delta \tau_y \sigma_y) \tilde{g}_\lambda(k, i\omega) \end{aligned}$$

and with the above, the electronic Gor'kov-Nambu Green's function becomes

$$\begin{aligned} \hat{G}(\mathbf{k}, i\omega) &= e^{-i\frac{\pi}{4} \hat{\mathbf{k}} \cdot \tilde{\boldsymbol{\sigma}}} [i\omega - \xi_k \tau_z - \alpha k \sigma_z + \Delta \tau_y \sigma_y]^{-1} e^{i\frac{\pi}{4} \hat{\mathbf{k}} \cdot \tilde{\boldsymbol{\sigma}}} \\ &= \sum_{\lambda=\pm} \frac{1 + \lambda(\hat{\mathbf{k}} \times \hat{\mathbf{z}}) \cdot \tilde{\boldsymbol{\sigma}}}{2} \frac{i\omega + \xi_{k\lambda} \tau_z}{(i\omega)^2 - \Delta^2 - \xi_{k\lambda}^2} \\ &\quad - \sum_{\lambda=\pm} \frac{1 + \lambda(\hat{\mathbf{k}} \times \hat{\mathbf{z}}) \cdot \tilde{\boldsymbol{\sigma}}}{2} \frac{\Delta \tau_y \sigma_y}{(i\omega)^2 - \Delta^2 - \xi_{k\lambda}^2}. \end{aligned} \quad (22)$$

Thus the presence of the Rashba SOC induces triplet pairing correlations [52–54]

$$\Delta(\hat{\mathbf{k}} \times \hat{\mathbf{z}}) \cdot \tilde{\boldsymbol{\sigma}} \tau_y \sigma_y = \Delta (\sin \varphi_{\mathbf{k}} \tau_x \sigma_z - \cos \varphi_{\mathbf{k}} \tau_y),$$

where $\tan \varphi_{\mathbf{k}} = k_y/k_x$. The emergence of triplet correlations can be also understood within the theory of induced orders and patterns of coexisting phases [53, 54, 56, 57]. In this work, we assume only a local pairing interaction leading to a spin singlet superconducting order parameter Δ [55], which is accompanied by the triplet correlations above. However, in the presence of suitable non-local interactions which contribute to the above superconducting triplet channel, the s-wave singlet and p-wave triplet order parameters *necessarily* coexist at a microscopic level due to the SOC [52–54]. In the latter case, a p-wave spin triplet order parameter has to be taken into account and determined self-consistently, as it can lead to modifications of the topological phase diagram [5].

In Eq. (22) one can identify the electronic Gor'kov-Nambu Green's function

$$G(\mathbf{k}, i\omega) = \sum_{\lambda=\pm} \frac{1 + \lambda(\hat{\mathbf{k}} \times \hat{\mathbf{z}}) \cdot \boldsymbol{\sigma}}{2} \frac{i\omega + \xi_{k\lambda}}{(i\omega)^2 - \Delta^2 - \xi_{k\lambda}^2}$$

and the anomalous one,

$$F(\mathbf{k}, i\omega) = \frac{\Delta}{2} \sum_{\lambda=\pm} \frac{i\sigma_y - \lambda(i \cos \varphi_{\mathbf{k}} + \sin \varphi_{\mathbf{k}} \sigma_z)}{(i\omega)^2 - \Delta^2 - \xi_{k\lambda}^2}.$$

By focusing on positions along the x axis, i.e. $\mathbf{r} = r \hat{\mathbf{x}}$, we find

$$\begin{aligned} \hat{G}(r \hat{\mathbf{x}}, i\omega) &= \int \frac{d\mathbf{k}}{(2\pi)^2} e^{ikr \cos \varphi_{\mathbf{k}}} \hat{G}(\mathbf{k}, i\omega) \\ &= \sum_{\lambda=\pm} \int_0^\infty \frac{dk k}{2\pi} \frac{J_0(kr) - i\lambda \sigma_y J_1(kr)}{2} \frac{i\omega + \tau_z \xi_{k\lambda} - \Delta \tau_y \sigma_y}{(i\omega)^2 - \Delta^2 - \xi_{k\lambda}^2}. \end{aligned} \quad (23)$$

These expressions are valid if $\omega_D \gg v_F/r \sim E_F/k_F r$, where ω_D is the Debye frequency. Mind that for $r = 0$, we basically recover the electronic bulk Green's function

$$\hat{G}(\mathbf{0}, i\omega) = -\pi\nu_F \frac{i\omega - \Delta\tau_y\sigma_y}{\sqrt{\omega^2 + \Delta^2}}. \quad (24)$$

B. RKKY interaction

In order to discuss the effective RKKY interaction mediated by the quasiparticles of a superconducting substrate with SOC, one can simply replace the Green's function appearing in Eq. (7) by the one of Eq. (23) and the spin Pauli matrices σ^α and σ^β by the corresponding components of the spin Pauli vector in the new representation $\tilde{\sigma} = (\tau_z\sigma_x, \sigma_y, \tau_z\sigma_z)$.

For a superconducting substrate, the RKKY interaction owes an additional term, which does not arise in the case of metallic substrates. This distinct RKKY term is associated with Shiba states [42], appearing due to the presence of the magnetic adatoms on the superconducting surface. The latter constitute localized states at the sites of the adatoms, with energies ε_0 which are smaller than the superconducting gap. In spite of the fact that the number of Shiba states is relatively small compared to the number of the bulk accessible states, it has been recently shown that their contribution to the RKKY interaction can become important, favoring an AFM ordering [58]. Nonetheless, in order for the Shiba term to dominate over the bulk RKKY contribution the adatom spacing has to be rather long, since the former decays as $(k_F r)^{-1}$ whereas the latter decays as $(k_F r)^{-2}$. The authors of Ref. [58] showed that the Shiba contribution dominates if the condition $k_F r > \xi_0/r$ is fulfilled, holding for the material parameters and the atomic spacing ($r \sim 100\text{nm}$), which they focused on.

In stark contrast, here we assume an adatom spacing of the order of 1 nm and a coherence length of $\xi_0 \sim 80\text{nm}$. Therefore we find that $k_F r < \xi_0/r$ and conclude that the Shiba bound state contribution is negligible in our case. Its inclusion would *only* move the phase boundaries slightly deeper into the AFM region. Moreover, since the main contribution to the RKKY interaction arises for energies quite above the gap Δ , there is also no quantitative modification of the results found previously in Sec. I for a normal metallic substrate. Therefore, the phase diagrams presented in Figs. 3 and 4, also hold for the case of a superconducting substrate.

III. EFFECTIVE MODEL FOR FM AND AFM SHIBA CHAINS

As we explained in the previous paragraph, the contribution of the Shiba states to the RKKY interaction is unimportant in the case under consideration, and thus their presence is irrelevant for deciding on the type of

magnetic order which will develop in the adatom chain. However, the Shiba states are midgap states which govern the low-energy behavior of the electronic degrees of freedom. Therefore, in this section we proceed with investigating the characteristics of the Shiba states that develop under the influence of background FM and AFM magnetic orderings of the adatom-spins \mathbf{S}_i , with $|\mathbf{S}_i| = S$, which have been stabilized by the effective RKKY interaction originating solely from the continuum spectrum. The magnetic exchange Hamiltonian now becomes

$$H_J = \frac{1}{2} \sum_{j=1}^N \iint \frac{d\mathbf{k}d\mathbf{k}'}{(2\pi)^2} e^{-i(\mathbf{k}-\mathbf{k}')\cdot\mathbf{R}_j} \psi_{\mathbf{k}}^\dagger M_j \tau_z \sigma_z \psi_{\mathbf{k}'} \quad (25)$$

with $\mathbf{R}_i = ia\hat{\mathbf{x}}$. We introduced $M_j = JS(\pm 1)^j$, corresponding to FM (+) and AFM (-) ordering, respectively. In order to find the electronic spectrum we solve the Bogoliubov - de Gennes (BdG) equation [27, 30, 31, 58–60]

$$\sum_j \int \frac{d\mathbf{k}'}{(2\pi)^2} \hat{G}(\mathbf{k}, \varepsilon) e^{-i(\mathbf{k}-\mathbf{k}')\cdot\mathbf{R}_j} M_j \tau_z \sigma_z \phi_{\mathbf{k}'} = \phi_{\mathbf{k}}, \quad (26)$$

where the wavefunction $\phi_{\mathbf{k}} = (u_{\mathbf{k}\uparrow}, u_{\mathbf{k}\downarrow}, v_{\mathbf{k}\uparrow}, v_{\mathbf{k}\downarrow})^T$ contains the spin-dependent particle- and hole-components u and v . We assume that the continuum states are *only slightly* affected by the presence of the magnetic atoms and thus assume the usual spectrum, $E_{\mathbf{k}} = \sqrt{\Delta^2 + \xi_{\mathbf{k}}^2}$, for the superconductor. By defining $\phi_j = (1/2\pi) \int d\mathbf{k} e^{i\mathbf{k}\cdot\mathbf{R}_j} \phi_{\mathbf{k}}$ we trace out the continuum states and end up with the equation

$$\sum_j \left[V_i \delta_{ij} - V_i \hat{G}(r_{ij}\hat{\mathbf{x}}, \varepsilon) V_j \right] \phi_j = 0, \quad (27)$$

where $V_j = M_j \tau_z \sigma_z$. By performing an expansion both in the normalized energy, ε/Δ , as well as the couplings to higher order neighbors, we obtain from Eq. (23)

$$\begin{aligned} \hat{G}(\mathbf{0}, \varepsilon) &\approx -\pi\nu_F(\varepsilon/\Delta - \tau_y\sigma_y), & (28) \\ \hat{G}(r\hat{\mathbf{x}}, \varepsilon) &\approx \mathcal{G}^s(r)\tau_z + \mathcal{G}^a(r)\tau_z\sigma_y \\ &\quad + \mathcal{F}^s(r)\tau_y\sigma_y + \mathcal{F}^a(r)\tau_y. & (29) \end{aligned}$$

The integrals in Eq. (23) together with the approximate form for the Bessel functions given in Eq. (A2), yield the coefficients

$$\frac{\mathcal{G}^s(r)}{\pi\nu_F} = \cos(m\alpha r) \sin(k_F|r| - \frac{\pi}{4}) e^{-\frac{|r|}{\xi_0}} \sqrt{\frac{2}{\pi k_F|r|}}, \quad (30)$$

$$\frac{\mathcal{F}^s(r)}{\pi\nu_F} = \cos(m\alpha r) \cos(k_F|r| - \frac{\pi}{4}) e^{-\frac{|r|}{\xi_0}} \sqrt{\frac{2}{\pi k_F|r|}}, \quad (31)$$

$$\frac{\mathcal{G}^a(r)}{i\pi\nu_F} = \sin(m\alpha r) \sin(k_F|r| - \frac{\pi}{4}) e^{-\frac{|r|}{\xi_0}} \sqrt{\frac{2}{\pi k_F|r|}}, \quad (32)$$

$$\frac{\mathcal{F}^a(r)}{i\pi\nu_F} = \sin(m\alpha r) \cos(k_F|r| - \frac{\pi}{4}) e^{-\frac{|r|}{\xi_0}} \sqrt{\frac{2}{\pi k_F|r|}}, \quad (33)$$

where ξ_0 is the coherence length of the superconductor. The indices s and a denote functions which are symmetric or anti-symmetric under inversion $r \rightarrow -r$. With this we rewrite Eq. (27) in the form of a Schrödinger equation

$$\sum_j \mathcal{H}_{ij} \phi_j = \varepsilon \phi_i \quad (34)$$

with the Hamiltonian

$$\mathcal{H}_{ij} = \frac{\Delta}{\pi \nu_F M^2} \left[(\pi \nu_F M^2 \tau_y \sigma_y - M_i \tau_z \sigma_z) \delta_{ij} + M_i M_j (\mathcal{G}_{i-j}^s \tau_z - \mathcal{G}_{i-j}^a \tau_z \sigma_y + \mathcal{F}_{i-j}^s \tau_y \sigma_y - \mathcal{F}_{i-j}^a \tau_y) \right], \quad (35)$$

where we have compactly denoted $f_{i-j} \equiv f(r_{ij})$ and set $M = JS$. The solution of Eq. (34) determines the energies and wavefunctions of the Shiba midgap states.

IV. TOPOLOGICAL FM SHIBA CHAIN

It has been well established, already from earlier proposals involving topological insulators [6] and semiconductors [8–11], that the combined presence of SOC, s-wave superconductivity and magnetism, can induce topological superconductivity. Note also that a recent symmetry classification [5] has presented further directions of how to combine these ingredients for engineering TSCs. Both cases of topological FM and AFM Shiba chains fall into this classification scheme. In fact, the effective model for a topological Shiba chain (see also [31]) resembles previous continuum models describing TSCs using nanowires with Rashba SOC [10, 11]. In the present case, the effective Zeeman field is provided by the magnetic adatoms (classical here) and the SOC occurs due to the involvement of a superconducting surface. However, there are also important differences. First, the perpendicular local magnetic field felt by the Shiba states is generally less harmful for superconductivity compared to a perpendicular magnetic field, due to the additional contribution of the orbital effects in the latter situation. In the case of Shiba states, in spite of the fact that the superconducting gap becomes locally suppressed, it generally survives even when the magnetic exchange energy becomes comparable to it [60]. In addition, note that the FM ordering is more likely to suppress superconductivity locally compared to the AFM ordering.

Moreover, another distinctive feature for the effective model of topological Shiba chains is that they incorporate triplet pairing correlations, which can generally lead to a significant quantitative modification of the phase diagram (see Ref. [5]). In addition, the topological Shiba chain models are lattice models involving higher order neighbor couplings, thus strongly depending on the adatom spacing. Consequently, one can not always restrict to a nearest neighbor model but instead, depending on the ratio ξ_0/a , a large number of neighbors can become relevant. Evenmore, the inherent presence of additional

chiral symmetries, leads to a rich variety of topologically phases even with 2 MFs per edge.

In the following paragraph, we first discuss the symmetries of a topological FM Shiba chain which are crucial for performing a topological classification of the accessible MF phases. Furthermore, we extract the topological phase diagram and study numerically the MF wavefunctions for a finite chain, in order to discuss aspects related to the experimental realization of this scenario.

A. Symmetry classification

As already mentioned, in the *absence* of magnetism, the point group symmetry of the hybrid structure (as in Fig. 1), consisting of the chain on top of an infinite substrate surface, is C_{2v} . Since the effective model describing the Shiba chains is embedded in the two-dimensional geometry, rather than being a strictly one dimensional system, it inherits the same point group properties. This is reflected in the C_{2v} point group symmetry of the non-magnetic part of the Hamiltonian in Eq. (35). This point group consists of the:

1. identity element $E : (x, y, z) \mapsto (x, y, z)$,
2. reflection operation $\sigma_{yz} : (x, y, z) \mapsto (-x, y, z)$,
3. reflection operation $\sigma_{xz} : (x, y, z) \mapsto (x, -y, z)$,
4. z axis π -rotation $C_2 : (x, y, z) \mapsto (-x, -y, z)$.

Note that for the effective Shiba state model of Eq. (35) only the inversion operation $\mathcal{I} : x \mapsto -x$ is accessible, and corresponds to $\mathcal{I}i = -i$ and $\mathcal{I}j = -j$, with i, j denoting adatom sites. Therefore, within our spinor formalism the aforementioned symmetries are generated by the unitary operators: $\hat{E} = I$, $\hat{\sigma}_{yz} = i\tau_z \sigma_x \mathcal{I}$, $\hat{\sigma}_{xz} = i\sigma_y$ and $\hat{C}_2 = i\tau_z \sigma_z \mathcal{I}$. The term associated with the presence of FM ordering, $M_j \tau_z \sigma_z = M \tau_z \sigma_z$, transforms under the C_{2v} elements in the following manner: $\hat{\sigma}_{yz}^\dagger \tau_z \sigma_z \hat{\sigma}_{yz} = -\tau_z \sigma_z$, $\hat{\sigma}_{xz}^\dagger \tau_z \sigma_z \hat{\sigma}_{xz} = -\tau_z \sigma_z$, $\hat{C}_2^\dagger \tau_z \sigma_z \hat{C}_2 = \tau_z \sigma_z$. Moreover, the FM chain is invariant under the action of the discrete translation operator, \hat{t}_a , which leads to shift $i \mapsto i + 1$, i.e. equal to the adatom spacing a .

In contrast, the usual time-reversal operation \mathcal{T} with generator $\hat{\mathcal{T}} = i\sigma_y \hat{\mathcal{K}}$, is broken as the FM term satisfies $\hat{\mathcal{T}}^\dagger \tau_z \sigma_z \hat{\mathcal{T}} = -\tau_z \sigma_z$. Here $\hat{\mathcal{K}}$ denotes the anti-unitary complex-conjugation operator. As it becomes evident from the above relations, the FM term is invariant under the action of the following combined symmetry operations: $\mathcal{T}\sigma_{xz}$ and $\mathcal{T}\sigma_{yz}$, i.e. consisting of operations under which the rest of the Hamiltonian is invariant. Usually, this type of symmetries are called *hidden* symmetries [5, 61], as they are a combination of symmetry operations which, separately, do not leave the Hamiltonian invariant. In the particular case only the action of the operator $\hat{\Theta} \equiv \hat{\sigma}_{xz} \hat{\mathcal{T}} = \hat{\mathcal{K}}$, which coincides with the complex conjugation, leaves the total BdG Hamiltonian invariant.

Similarly to the usual time-reversal symmetry operator \hat{T} , $\hat{\Theta}$ is also anti-unitary. We may thus call it a *generalized* time-reversal symmetry operator [5]. However, the operators differ in periodicity, i.e. $\hat{T}^2 = -I$ and $\hat{\Theta}^2 = I$. The latter implies that \mathcal{T} -symmetry will lead to a Kramers degeneracy, while Θ -symmetry imposes a reality condition on the Hamiltonian without any Kramers pairs [62–64]. In the case under consideration, the presence of Θ -symmetry together with the built-in charge-conjugation symmetry of the BdG Hamiltonian, effected by the operator $\hat{\Xi} \equiv \tau_x \hat{\mathcal{K}}$, give rise to the chiral symmetry operator $\hat{\Pi} \equiv \tau_x$. Thus although the usual time-reversal symmetry is broken in our system, the presence of the aforementioned set of symmetries implies that the system resides in the BDI symmetry class, which in one dimension can support topologically non-trivial phases characterized by a \mathbb{Z} invariant [62–64]. The latter allows an integer number of MFs per chain edge (see also [43–46]). As we show in the next paragraph these topological phases are indeed accessible with the particular system.

B. FM Shiba chain Hamiltonian

In order to study the topological properties of a FM Shiba chain, we will transfer to momentum space, defined in the FM Brillouin zone (BZ) $k \in (-\pi/a, \pi/a]$. At this point we introduce the corresponding BdG momentum space Hamiltonian, $\mathcal{H}_k = \mathcal{H}_k^0 + \mathcal{H}_k^m$, consisting of the **i.** non-magnetic \mathcal{H}_k^0 and **ii.** magnetic \mathcal{H}_k^m parts:

$$\mathcal{H}_k^0 = t_k \tau_z - v_k \tau_z \sigma_y + (\Delta + \mathcal{D}_k) \tau_y \sigma_y - d_k \tau_y, \quad (36)$$

$$\mathcal{H}_k^m = -\mathcal{B} \tau_z \sigma_z, \quad (37)$$

where we have introduced $\mathcal{B} = \Delta/(\pi\nu_F JS)$ and

$$t_k = \sum_{\delta=1}^{\infty} t_{\delta} \cos(\delta ka) \quad \text{with} \quad t_{\delta} = \frac{2\Delta}{\pi\nu_F} \mathcal{G}_{\delta}^s, \quad (38)$$

$$v_k = \sum_{\delta=1}^{\infty} v_{\delta} \sin(\delta ka) \quad \text{with} \quad v_{\delta} = \frac{2\Delta}{i\pi\nu_F} \mathcal{G}_{\delta}^a, \quad (39)$$

$$\mathcal{D}_k = \sum_{\delta=1}^{\infty} \mathcal{D}_{\delta} \cos(\delta ka) \quad \text{with} \quad \mathcal{D}_{\delta} = \frac{2\Delta}{\pi\nu_F} \mathcal{F}_{\delta}^s, \quad (40)$$

$$d_k = \sum_{\delta=1}^{\infty} d_{\delta} \sin(\delta ka) \quad \text{with} \quad d_{\delta} = \frac{2\Delta}{i\pi\nu_F} \mathcal{F}_{\delta}^a. \quad (41)$$

The above Hamiltonian acts on the wavefunction $\phi_k = (u_{k\uparrow}, u_{k\downarrow}, v_{k\uparrow}, v_{k\downarrow})^T$. In addition, t_{δ} corresponds to the δ -order nearest neighbor hopping, v_{δ} corresponds to the δ -order nearest neighbor SOC, \mathcal{D}_{δ} to the δ -order nearest neighbor extended s-wave spin-singlet superconducting gap and d_{δ} to the δ -order nearest neighbor spin-triplet superconducting gap oriented along the y axis.

C. Topological invariant

For exploring the topological phase diagram, we reside on the presence of chiral symmetry $\hat{\Pi} = \tau_x$ and block off-diagonalize the BdG Hamiltonian [43, 64], via a rotation about the τ_y axis effected by the unitary transformation $(\tau_z + \tau_x)/\sqrt{2}$. We obtain

$$\mathcal{H}'_k = \begin{pmatrix} 0 & A_k \\ A_k^{\dagger} & 0 \end{pmatrix}. \quad (42)$$

The upper block off-diagonal block is given by

$$A_k = t_k - id_k - \mathcal{B} \sigma_z - [v_k - i(\Delta + \mathcal{D}_k)] \sigma_y. \quad (43)$$

The determinant of A_k is a complex number and reads

$$\begin{aligned} \text{Det}[A_k] &= t_k^2 + (\Delta + \mathcal{D}_k)^2 - \mathcal{B}^2 - d_k^2 - v_k^2 \\ &+ 2i[v_k(\Delta + \mathcal{D}_k) - t_k d_k]. \end{aligned} \quad (44)$$

With the vectors $\mathbf{g}_k = (\text{Re Det}[A_k], \text{Im Det}[A_k], 0)$ and $\hat{\mathbf{g}}_k = \mathbf{g}_k/|\mathbf{g}_k|$, the related \mathbb{Z} topological invariant is defined by the winding number [30, 65]

$$\mathcal{N} = \frac{1}{2\pi} \int_{BZ} dk \left(\hat{\mathbf{g}}_k \times \frac{\partial \hat{\mathbf{g}}_k}{\partial k} \right)_z. \quad (45)$$

Note that by considering a \mathbb{Z} classification which also takes into account phases with 2 MFs, we manage to go beyond the study of a FM Shiba chain performed in Ref. [31], which assumed a \mathbb{Z}_2 classification and thus restricted to the cases with 1 MF per edge.

D. Topological phase diagram – Results

In Fig. 6 we show the winding number as a function of the adatom spacing a , magnetic exchange energy JS and SOC strength α . Phases with zero, one or two MFs per edge are accessible. When the ground state of the system resides in a phase near a boundary of the topological phase diagram, one can employ a weak perpendicular Zeeman (electric) field to tune the magnetic exchange energy (SOC strength) in order to achieve transitions between phases with different number of MFs. We additionally observe in Fig. 6(b) that the phase diagram exhibits MF bound states even for *very small* values of α . This is similar to the nanowire case [10, 11], where α mainly determines the spatial profile and localization of the MFs at the edges of a finite system. Interestingly, this also holds for the case of 2 MFs per edge.

In Fig. 7 we compare the winding number calculation shown in panel (a), with the evolution of the two lowest positive eigenenergies, shown in panel (b) that was obtained from the open chain Hamiltonian for different lengths. As follows from bulk-boundary correspondence, the number of MF bound states agrees with the value of \mathcal{N} , although long chains are required here in order to obtain quantitative accordance with the predicted phase

boundaries. As a matter of fact, this is the case for the gap closing that occurs at the transition from trivial to $\mathcal{N} = 2$. Here, two truly-zero energy bound states appear only for very long chains. This has to be contrasted with the region where $\mathcal{N} = 1$. There, the zero energy bound state become stabilized already for shorter lengths of the chain, which can be seen through the different decays of the wavefunctions in Fig. 8(a) and (b).

To shed more light on the above findings, we complementary demonstrate in Fig. 7(c) the gap closings of the bulk band structure, for the parameters where the topological quantum phase transitions occur. One observes that the phase transition involving a single MF corresponds to gap closings at the inversion symmetric wavevector $k = 0$, whereas in the case involving 2MFs, the dispersion shows gap closings at two non-inversion-symmetric points $\pm k_*$.

For even better understanding, let us investigate in more detail the behavior of the topological invariant. The gap closing conditions and therefore the phase boundaries, are given by setting $\text{Det}[A_k] = 0$, which requires the following two equations to be simultaneously satisfied

$$v_k(\Delta + \mathcal{D}_k) - t_k d_k = 0, \quad (46)$$

$$t_k^2 + (\Delta + \mathcal{D}_k)^2 - \mathcal{B}^2 - d_k^2 - v_k^2 = 0. \quad (47)$$

To obtain some analytical results, we will focus on a simplified situation. For instance, by considering a short superconducting coherence length, ξ_0 , we can restrict ourselves only up to nearest neighbor terms in the Hamiltonian of Eq. (36). Under these conditions we have $t_k = t_1 \cos(ka)$, $v_k = v_1 \sin(ka)$, $\mathcal{D}_k = \mathcal{D}_1 \cos(ka)$ and

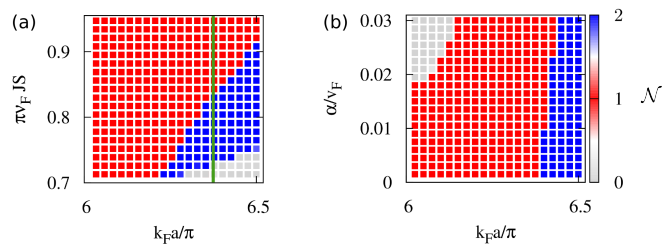


Figure 6: The \mathbb{Z} topological invariant (winding number) as defined in Eq. (45), for varying adatom spacing a and (a) magnetic exchange energy JS ($\alpha = 0.01 v_F$) or (b) normalized SOC strength α ($\pi v_F JS = 0.85$). In both cases, we find topological phases harboring 1 or 2 MFs per chain edge. Note in (a) that tuning the magnetic exchange energy can be used to switch between 1 and 2 MF phases. When close to the phase boundary, the latter could be for instance achieved by applying a weak perpendicular Zeeman field. In (b) we observe that for an infinitesimally small SOC strength, both 1 and 2 MF phases are accessible. This is anticipated for the single MF phase where α does not enter the topological criterion, but quite remarkably, it also takes place for the 2 MF situation. Here electrical tuning of α can be used for realizing topological quantum phase transitions.

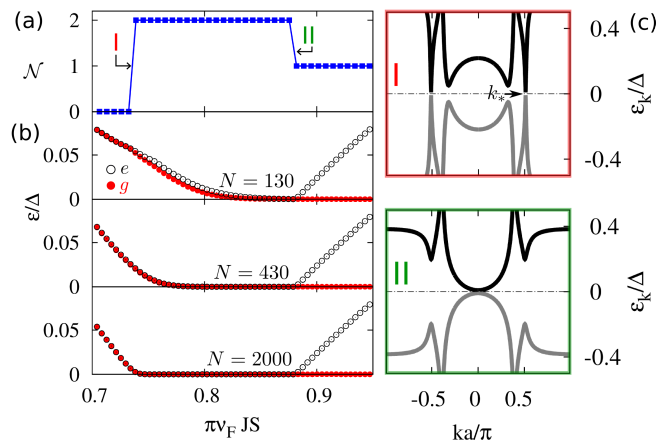


Figure 7: (a) The \mathbb{Z} topological invariant (winding number) as defined in Eq. (45) (blue) depending on the magnetic exchange energy JS along the green line in Fig. 6(a). (b) The two lowest positive eigenenergies in red and black for three different lengths of the chain ($N = 130$, $N = 430$ and $N = 2000$). Note that in order to obtain well localized MF bound states and validate the bulk-boundary correspondence predictions, quite long chains are required. This is particularly the case for the transition to the 2 MF phase, which is protected by chiral symmetry. In panel (c) we show the corresponding gap closings of the energy dispersions ε_k , occurring exactly at the phase transition points **I** and **II**. The transition (**I**) $\mathcal{N} = 0 \rightarrow 2$ arises from gap closings at the non-inversion-symmetric points $\pm k_*$, connected to each other by inversion. Instead, the transition (**II**) $\mathcal{N} = 2 \rightarrow 1$ arises due to a gap closing at the inversion symmetric momentum $k = 0$.

$d_k = d_1 \sin(ka)$. Eq. (46) is satisfied for the inversion symmetric points $k = 0, \pi$ and the pair of non-inversion-symmetric points $\pm k_*$, given by $\cos(k_* a) = v_1 \Delta / (d_1 t_1 - v_1 \mathcal{D}_1)$. By setting these k -values in Eq. (47), we obtain the gap closing conditions, or equivalently the phase boundaries. For $k = 0, \pi$ we obtain the condition $t_1^2 + (\Delta \pm \mathcal{D}_1)^2 = \mathcal{B}^2$, akin to the criteria found in nanowire models [10, 11]. A similar procedure can provide the gap closing conditions for $\pm k_*$ points, which however is quite lengthy and will not be presented here.

It is important to comment on the form of the wavefunctions in the case of 2 MFs. In this case, the non-inversion-symmetric points $\pm k_*$, will give rise to zero-energy wavefunctions, which however are complex and proportional to $e^{\pm i k_* a j}$ (j index of chain site). Nonetheless, MF wavefunctions should be real, and this can only be achieved by making linear combinations of the wavefunctions, so that they finally obtain a dependence $\cos(k_* a j)$ and $\sin(k_* a j)$. This explains **i.** the oscillating behavior shown in Fig. 8 with a period determined by k_* and **ii.** the fact that when one MF wavefunction shows a maximum, the other shows a minimum. As expected, the MF wavefunction for a single MF phase does not show this type of feature.

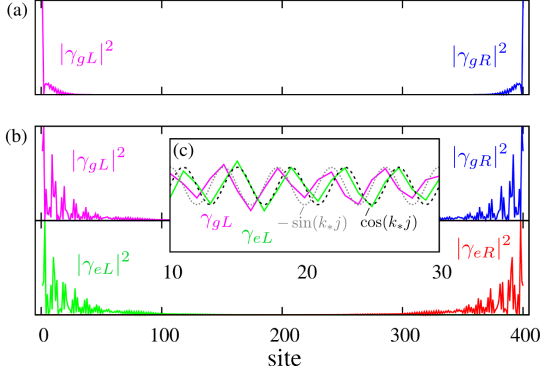


Figure 8: Wavefunctions corresponding to Fig. 7 for the ground state (g) and the first excited state (e). The left and right Majorana bound states are labeled by (L) and (R), respectively. (a) Whereas the MF wavefunction within the 1MF phase is strongly localized and oscillates with a periodicity of lattice spacing, panel (b) shows the wavefunctions inside the 2MF phase which strongly leak into the bulk and oscillate with a wavenumber k_* .

V. TOPOLOGICAL AFM SHIBA CHAIN

The presence of Rashba SOC due to the superconducting substrate, is an ingredient capable of engineering MFs also for other magnetic phases of the chain, apart from the FM one. As we already discussed in previous paragraphs, the same conditions which favor the FM ordering, also provide fertile ground for the establishment of AFM ordering. A crucial requirement is the presence of strong Ising anisotropy in order to overcome the DM interaction. If this is the case, other details such as the adatom spacing, will decide on the FM or AFM type of ordering.

The possibility of topological AFM Shiba chains was recently discussed in Ref. [30] for superconducting substrates in the absence of SOC. In that case, a new mechanism for engineering topological superconductivity was proposed, where SOC was induced by a supercurrent flow along the chain together with an in plane Zeeman field. Note that AFM and FM Shiba chains can only host MFs in the presence of some kind of SOC [5]. In stark contrast, spiral Shiba chains do not require SOC, but exhibit MF in a self-tuned manner. Nonetheless, any realistic manipulation of MFs in spiral Shiba chains will unavoidably require the application of external Zeeman fields [28] or supercurrents [29], counterbalancing the advantage of self-tunability.

In the rest of the manuscript we will focus on the topological phases supported in AFM Shiba chains. As we will present in the next paragraphs, some of the generic results which we reported earlier for the FM case are also relevant for the AFM order. For instance, AFM Shiba chains also support MF phases with one or two MFs per chain edge. However, as we explain in the AFM analy-

sis, the underlying mechanism and the topologically relevant k -space points, differ in each case. The reason can be traced back to the **i.** different magnetic wavevector $Q = 0$ or π and **ii.** the presence of additional *hidden* symmetries which appear in the AFM case.

A. Symmetry classification

The present paragraph follows closely the analysis carried out for the FM case. As previously, the relevant point group in the absence of magnetism is C_{2v} . The Hamiltonian of Eq. (35) includes now the AFM term, given by $M_j \tau_z \sigma_z = M(-1)^j \tau_z \sigma_z$. The latter AFM Hamiltonian term, transforms under the C_{2v} elements in the following manner: $\hat{\sigma}_{yz}^\dagger (-1)^j \tau_z \sigma_z \hat{\sigma}_{yz} = -(-1)^j \tau_z \sigma_z$, $\hat{\sigma}_{xz}^\dagger (-1)^j \tau_z \sigma_z \hat{\sigma}_{xz} = -(-1)^j \tau_z \sigma_z$ and $\hat{C}_2^\dagger (-1)^j \tau_z \sigma_z \hat{C}_2 = (-1)^j \tau_z \sigma_z$. Essentially, we recover exactly the same behavior encountered in the FM case, since $\mathcal{I}(-1)^j = (-1)^{-j} = (-1)^j$. However, in contrast to the FM ordering, the AFM chain is invariant under the translation operation, t_{2a} , instead of t_a . Thus the reduced Brillouin zone (RBZ) becomes now relevant, defined by $k \in (-\pi/2a, \pi/2a]$. This reflects the formation of a two sublattice structure. With the help of the translation operator, \hat{t}_a , we additionally obtain $\hat{t}_a^\dagger (-1)^j \tau_z \sigma_z \hat{t}_a = -(-1)^j \tau_z \sigma_z$. Finally, similarly to the FM case, the system is not invariant under \mathcal{T} , as $\hat{\mathcal{T}}^\dagger (-1)^j \tau_z \sigma_z \hat{\mathcal{T}} = -(-1)^j \tau_z \sigma_z$.

As in the FM case, the AFM chain is invariant under the hidden symmetry operator $\hat{\Theta} \equiv \hat{\sigma}_{xz} \hat{\mathcal{T}} = \hat{\mathcal{K}}$. More importantly, the distinct property $\hat{t}_a^\dagger (-1)^j \tau_z \sigma_z \hat{t}_a = -(-1)^j \tau_z \sigma_z$ can yield additional hidden symmetries, when t_a is combined with σ_{yz} , σ_{xz} or \mathcal{T} . Indeed we find three additional symmetries: **i.** the anti-unitary symmetry $\Theta' = \mathcal{T} t_a$ **ii.** the unitary symmetry $\mathcal{O} = \sigma_{xz} t_a$ and **iii.** the unitary symmetry $\mathcal{O}' = \sigma_{yz} t_a$. On the other hand, unitary symmetries allow to block-diagonalize the Hamiltonian and label it with the eigenvalues of the respective operators. Here we may use only one of the two unitary symmetry operators for block diagonalizing the Hamiltonian. Note that the presence of two anti-unitary symmetries Θ and Θ' , does not allow the classification of the Hamiltonian according to the ten existing symmetry classes [62–64]. The latter classification methods can be *only* applied on Hamiltonians with no additional unitary symmetries present. However, after the block diagonalization of the Hamiltonian relying on the unitary symmetry, a symmetry classification is possible [5]. This is exactly the tactic which we will follow in the next paragraph, by first transferring to the RBZ.

B. AFM Shiba chain Hamiltonian

By transferring to momentum space, we obtain the following Schrödinger equation, which provides the single-

particle spectrum in the AFM case:

$$\mathcal{H}_k^0 \phi_k + \mathcal{H}_k^m \phi_{k+Q} = \varepsilon \phi_k, \quad (48)$$

with $Q = \pi/a$, $k \in \text{BZ}$, \mathcal{H}_k^0 and \mathcal{H}_k^m given in Eq. (36). By passing to the RBZ we obtain

$$\begin{pmatrix} \mathcal{H}_{k-Q/2}^0 & \mathcal{B}\tau_z\sigma_z \\ \mathcal{B}\tau_z\sigma_z & \mathcal{H}_{k+Q/2}^0 \end{pmatrix} \begin{pmatrix} \phi_{k-Q/2} \\ \phi_{k+Q/2} \end{pmatrix} = \varepsilon \begin{pmatrix} \phi_{k-Q/2} \\ \phi_{k+Q/2} \end{pmatrix}, \quad (49)$$

where by additionally introducing the $\boldsymbol{\rho}$ Pauli matrices in the AFM space we end up with the Hamiltonian

$$\tilde{\mathcal{H}}_k = \mathcal{H}_{k,+}^0 + \mathcal{H}_{k,-\rho_z}^0 + \mathcal{B}\tau_z\rho_x\sigma_z \quad (50)$$

defined in the RBZ, while we introduced

$$\mathcal{H}_{k,\pm}^0 = \frac{\mathcal{H}_{k-Q/2}^0 \pm \mathcal{H}_{k+Q/2}^0}{2}. \quad (51)$$

The explicit form reads

$$\begin{aligned} \tilde{\mathcal{H}}_k &= t_{k,+}\tau_z + t_{k,-}\tau_z\rho_z - v_{k,+}\tau_z\sigma_y - v_{k,-}\tau_z\rho_z\sigma_y \\ &+ (\Delta + \mathcal{D}_{k,+})\tau_y\sigma_y + \mathcal{D}_{k,-}\tau_y\rho_z\sigma_y - d_{k,+}\tau_y - d_{k,-}\tau_y\rho_z \\ &- \mathcal{B}\tau_z\rho_x\sigma_z, \end{aligned} \quad (52)$$

where the parameters appearing can be directly retrieved by the definitions of t_k , v_k , \mathcal{D}_k and d_k . For completeness, we present their expression below

$$t_{k,+} = \sum_{l=1}^{\infty} t_{2l} \cos(2lka) (-1)^l, \quad (53)$$

$$t_{k,-} = \sum_{l=1}^{\infty} t_{2l-1} \sin[(2l-1)ka] (-1)^l, \quad (54)$$

$$v_{k,+} = \sum_{l=1}^{\infty} v_{2l} \sin(2lka) (-1)^l, \quad (55)$$

$$v_{k,-} = \sum_{l=1}^{\infty} v_{2l-1} \cos[(2l-1)ka] (-1)^{l+1}, \quad (56)$$

$$\mathcal{D}_{k,+} = \sum_{l=1}^{\infty} \mathcal{D}_{2l} \cos(2lka) (-1)^l, \quad (57)$$

$$\mathcal{D}_{k,-} = \sum_{l=1}^{\infty} \mathcal{D}_{2l-1} \sin[(2l-1)ka] (-1)^l, \quad (58)$$

$$d_{k,+} = \sum_{l=1}^{\infty} d_{2l} \sin(2lka) (-1)^l, \quad (59)$$

$$d_{k,-} = \sum_{l=1}^{\infty} d_{2l-1} \cos[(2l-1)ka] (-1)^{l+1}. \quad (60)$$

At this point, we move on with the symmetry classification. In the particular basis, the translation operator \hat{t}_a has the representation

$$\hat{t}_a = \begin{pmatrix} e^{i(k-Q/2)a} & 0 \\ 0 & e^{i(k+Q/2)a} \end{pmatrix} = -i\rho_z e^{ika}. \quad (61)$$

For simplicity, we will drop the $U(1)$ phase factor, since it is irrelevant for the present discussion. On the other hand, complex conjugation has the following representation in this basis $\hat{\mathcal{K}} = \rho_x \hat{\mathcal{K}}'$, with $\hat{\mathcal{K}}'$ not acting on the wavevector Q . Under these conditions we obtain the representation for the following operators: $\hat{\Theta} = \rho_x \hat{\mathcal{K}}'$, $\hat{\Theta}' = \rho_y \sigma_y \hat{\mathcal{K}}'$ and $\hat{\mathcal{O}} = \rho_z \sigma_y$. We directly confirm that the Hamiltonian is invariant under the action of these operators, as discussed in the previous paragraph. However, there are additional symmetries. We find two chiral symmetries: $\hat{\Pi} \equiv \tau_x$ and $\hat{\tilde{\Pi}} \equiv \tau_x \rho_z \sigma_y$, as also two charge-conjugation symmetries: $\hat{\Xi} \equiv \tau_x \rho_x \hat{\mathcal{K}}'$ and $\hat{\tilde{\Xi}} \equiv \tau_x \rho_y \sigma_y \hat{\mathcal{K}}'$. In this representation both time-reversal symmetry operators satisfy $\hat{\Theta}^2 = (\hat{\Theta}')^2 = I$, yielding the symmetry class $\text{BDI} \oplus \text{BDI}$.

The particular symmetry class of the Hamiltonian can alternatively be retrieved by block diagonalizing the Hamiltonian via the transformation

$$U = \frac{\rho_y + \rho_z}{\sqrt{2}} \frac{\rho_z \sigma_z + \sigma_y}{\sqrt{2}} e^{-i\frac{\pi}{4}\sigma_y}, \quad (62)$$

which yields $U \tilde{\mathcal{H}}_k U^\dagger = \frac{1}{2} \sum_{\sigma} (1 + \sigma \sigma_z) \otimes \tilde{\mathcal{H}}_{k,\sigma}$, with the blocks

$$\begin{aligned} \tilde{\mathcal{H}}_{k,\sigma} &= (t_{k,+} - \sigma v_{k,-})\tau_z + (t_{k,-} - \sigma v_{k,+})\tau_z\rho_y + \mathcal{B}\tau_z\rho_z \\ &+ [\sigma(\Delta + \mathcal{D}_{k,+}) - d_{k,-}]\tau_y\rho_y + (\sigma\mathcal{D}_{k,-} - d_{k,+})\tau_y. \end{aligned} \quad (63)$$

Interestingly we find that for each subspace, σ up and down, the Hamiltonian possesses the form of two decoupled topological FM Shiba chain models (see Eq. (36)), but with the AFM Pauli matrices playing the role of the spin Pauli matrices. Note, that with the particular choice of the spinor, the functions in front of the matrices have a similar behavior under inversion ($k \rightarrow -k$), as in the FM Shiba case studied earlier or related nanowire models [10, 11, 32, 43]. Therefore, we anticipate at least an equally rich phase diagram, exhibiting an interplay of topological phases with one or two MFs per edge of the chain.

C. Topological invariant

Each of the σ subblocks reside in the BDI symmetry class and can be off-block diagonalized, similar to the procedure followed in the FM case. Therefore, we effect the transformation $(\tau_z + \tau_x)/(\sqrt{2})$ which yields

$$\tilde{H}'_{k,\sigma} = \begin{pmatrix} 0 & A_{k,\sigma} \\ A_{k,\sigma}^\dagger & 0 \end{pmatrix}, \quad (64)$$

with the upper off-diagonal block given by

$$\begin{aligned} A_{k,\sigma} &= t_{k,+} - \sigma v_{k,-} + i(d_{k,+} - \sigma\mathcal{D}_{k,-}) + \mathcal{B}\rho_z \\ &- \{\sigma v_{k,+} - t_{k,-} - i[\sigma(\Delta + \mathcal{D}_{k,+}) + d_{k,-}]\}\rho_y. \end{aligned} \quad (65)$$

By introducing the determinants $\text{Det}[A_{k,\sigma}]$, as also the related vectors $\mathbf{g}_{k,\sigma} = (\text{Re Det}[A_{k,\sigma}], \text{Im Det}[A_{k,\sigma}], 0)$, we can define the quantities

$$\mathcal{N}_\sigma = \frac{1}{2\pi} \int_{RBZ} dk \left(\hat{\mathbf{g}}_{k,\sigma} \times \frac{\partial \hat{\mathbf{g}}_{k,\sigma}}{\partial k} \right)_z, \quad (66)$$

with the unit vectors $\hat{\mathbf{g}}_{k,\sigma} = \mathbf{g}_{k,\sigma}/|\mathbf{g}_{k,\sigma}|$. However, the quantities above *do not* constitute topological invariants because the $\mathbf{g}_{k,\sigma}$ vectors are not compactified in the RBZ, i.e. do not have the same value for the RBZ edges $k = \pm\pi/2a$. The latter occurs because we chose to work in the AFM space $\{k-Q/2, k+Q/2\}$, instead of the band-index space. Only Hamiltonians defined in the band index space satisfy the compactification condition. In the present situation, the folding of k -space has been performed in a convenient manner, which however does not meet the above criterion. Therefore, a topological invariant can be only defined by combining the two σ sectors. Essentially we have to start from the total Hamiltonian $\tilde{\mathcal{H}}_k$, block off-diagonalize it, introduce the upper off-diagonal block \tilde{A}_k and define a corresponding vector $\tilde{\mathbf{g}}_k = (\text{Re Det}[\tilde{A}_k], \text{Im Det}[\tilde{A}_k], 0)$. This procedure yields the topologically invariant quantity

$$\mathcal{N} = \mathcal{N}_\uparrow + \mathcal{N}_\downarrow \quad (67)$$

with \mathcal{N}_σ being \mathbb{R} , instead of \mathbb{Z} . Note this procedure was circumvented in Ref. [30] by extending the integration to the BZ. However, the method presented in this paragraph is the most general and we conclude that *only* \mathcal{N} is capable of providing the related \mathbb{Z} number of MFs per edge which are protected by chiral symmetry.

Nonetheless, there can be situations where additional terms in the Hamiltonian can violate chiral symmetry while at the same time preserving the unitary symmetry \mathcal{O} . In this case, each Hamiltonian block $\tilde{\mathcal{H}}_{k,\sigma}$ belongs to symmetry class D, which is characterized by a strong \mathbb{Z}_2 invariant in one momentum space dimension. However, due to interdependence of the two blocks, only phases with 0 or 1 MFs are accessible. The phase diagram is retrieved by introducing a total \mathbb{Z}_2 invariant obtained by multiplying the \mathbb{Z}_2 invariants of each block.

D. Topological phase diagram – Results

In Fig. 9 we present the calculated winding number \mathcal{N} of Eq. (67), with varying adatom spacing a and (a) magnetic exchange energy $\pi\nu_F JS$ or (b) normalized SOC strength α . As in the FM case, we also encounter phases with zero, one or two MFs per edge. The modification of the magnetic exchange energy, effected for instance by applying of a Zeeman field perpendicular to the ordered spins (x axis), can tune the phase diagram. Similar functionality appears with the variation of the SOC strength, where its increase can extend the window for phases with 2 MFs.

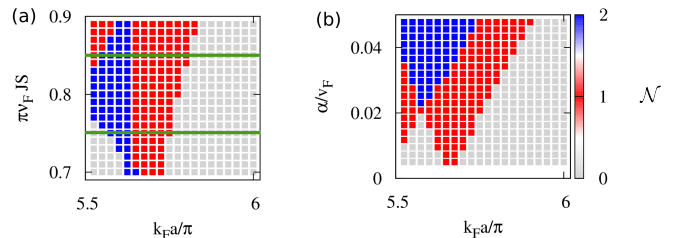


Figure 9: The \mathbb{Z} topological invariant (winding number) as defined in Eq. (67), for varying adatom spacing a and (a) magnetic exchange energy JS ($\alpha = 0.03 v_F$) or (b) normalized SOC strength α ($\pi\nu_F JS = 0.85$). In both cases, we find topological phases harboring 1 or 2 MFs per chain edge. Note in (a), that tuning the magnetic exchange energy can be used to switch between 1 and 2 MF phases. When close to the phase boundary, this could be achieved with a weak perpendicular Zeeman field (x axis). Observe also that a threshold SOC strength is generally required for both 1 and 2 MF phases to become accessible. This is in contrast to the FM case and arises because the strength for the SOC α appears now in the topological criterion for the 1MF phase. Therefore, also tuning of α can be exploited for realizing topological quantum phase transitions, but via a different mechanism.

However, in contrast to the FM case, we observe that *generally* a critical SOC strength is required for realizing a transition to the topological phases. The latter feature will be explained below, by considering a nearest neighbor model for the AFM Shiba chain. In short, the apparent difference relies on the fact that for the 1MF phase of the FM and AFM chains, different k points are topologically involved. For the FM case, the inversion-symmetric points $k = 0, \pi$ become relevant. In contrast, the 1MF phase in the AFM case arise from gap closings of each $\sigma = \uparrow, \downarrow$ block Hamiltonian at the $k = 0$ point of the RBZ, which coincides with the $\pi/2a$ point of the original BZ. Therefore, the topological criteria are retrieved from different points, with the SOC strength not involved in the FM case but crucially appearing in the AFM case.

We now proceed with examining in more detail the topological properties of the system for two values of the magnetic exchange energy. First we consider a cut of Fig. 9 for $\alpha = 0.03 v_F$ and $\pi\nu_F JS = 0.75$. In Fig. 10 we present: (a) the topological invariant \mathcal{N} and (b) the relevant gap closings in RBZ associated with the changes of \mathcal{N} . We observe in Fig. 10(b) that the transition $\mathcal{N} = 0 \rightarrow 2$ occurs due to the gap closings at the points $\pm k_*$ for $\sigma = \downarrow$. The particular phase with 2MFs is protected by chiral symmetry. Upon increasing the adatom distance in phase II, the $\pm k_*$ points converge to $k = 0$ and merge, exactly when another topological phase transition occurs $\mathcal{N} = 2 \rightarrow 1$. The latter transition and change in \mathcal{N} is possible due to the recombination of the two $\pm k_*$ points at the inversion symmetric point $k = 0$ of the RBZ. The last transition to the trivial superconducting phase occurs via a gap closing at $k = 0$ of the

$\sigma = \downarrow$ subblock. Note generally that the dependence of \mathcal{N} on the adatom spacing a is quite complicated, as all the coefficients are functions of the latter. In Fig. 10(c) we depict the two-lowest positive eigenenergies of the AFM Hamiltonian for an open chain. Note that, the appearance of a single zero eigenenergy agrees very well with the bulk predictions for the 1MF phase. In contrast, the bulk results for the 2MF phase are retrieved for quite long chains.

In Fig. 11 we present the arising MF wavefunctions in the 1 MF and 2 MF cases. In the case with 2 MFs, we retrieve once again the oscillatory behavior of the wavefunctions associated with the $\cos(k_*aj)$ and $\sin(k_*aj)$, related to chiral symmetry. However, the MF wavefunction for the 1MF phase, shows also a particular oscillatory behaviour due to different reasons. Since the latter topological phase is arising from the $k = 0$ point of the RBZ, which coincides with the $k = \pi/2a$ point of the BZ, the wavefunctions show close to this transition point a characteristic oscillatory behavior given by the lattice constant, i.e. it assumes the form $\cos(j\pi/2)$. This oscillatory behavior, with a wavelength given by the adatom spacing, still persists even deep inside the 1MF phase (see Fig. 11(a)).

To obtain further insight, we will retrieve some analytical results by restricting to the nearest and next nearest neighbor versions of the Hamiltonian in Eq. (36). For the nearest neighbor model we have $t_k = t_1 \cos(ka)$, $v_k = v_1 \sin(ka)$, $\mathcal{D}_k = \mathcal{D}_1 \cos(ka)$ and $d_k = d_1 \sin(ka)$. Each Hamiltonian block now obtains the form

$$\begin{aligned} \tilde{\mathcal{H}}_{k,\sigma} = & -\sigma v_1 \cos(ka) \tau_z - t_1 \sin(ka) \tau_z \rho_y + \mathcal{B} \tau_z \rho_z \\ & + [\sigma \Delta - d_1 \cos(ka)] \tau_y \rho_y - \sigma \mathcal{D}_1 \sin(ka) \tau_y. \end{aligned} \quad (68)$$

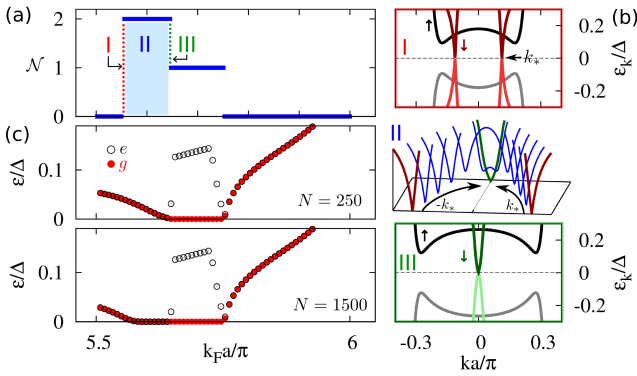


Figure 10: (a) The invariant \mathcal{N} as defined in Eq. (67) along the green line in Fig. 9(a) for $\pi\nu_F JS = 0.75$. (b) We depict the energetically lowest dispersions corresponding to the two blocks $\sigma = \uparrow, \downarrow$ of the Hamiltonian in Eq. (63), at the transition points where $\mathcal{N} = 0 \rightarrow 2$ (I) and $\mathcal{N} = 2 \rightarrow 1$ (III). Inbetween the two critical spacings, corresponding to (I) and (III), the previous gap closing points $\pm k_*$ move towards $k = 0$ (II). (c) Ground state energy (red dots) and first excited energy (black) depending on a for a chain length of $N = 250$ and $N = 1500$ atoms.

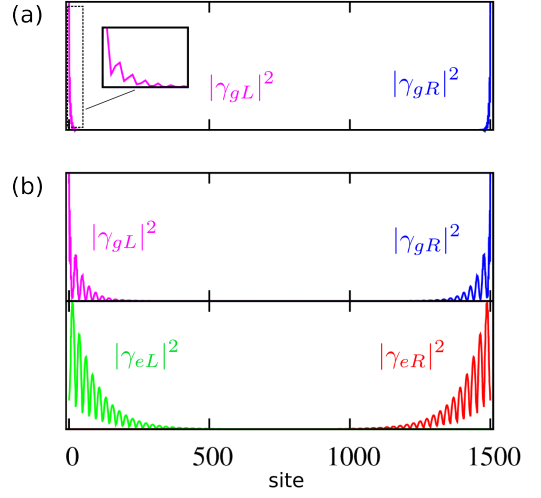


Figure 11: Majorana wavefunctions corresponding to Fig. 10 for the ground state (g) and the first excited state (e). The left and right Majorana bound states are labeled by (L) and (R) respectively. (a) The MF wavefunction in the 1MF phase shows an oscillatory dependence on the lengthscale of the adatom spacing. (b) The wavefunctions inside the 2MF phase are less localized and oscillate with an inverse wavelength k_* .

The apparent exchange of roles between $t_1 \leftrightarrow v_1$ and $\mathcal{D}_1 \leftrightarrow d_1$ happens because the $k = 0$ point of the RBZ corresponds to the $k = \pi/2a$ of the BZ. This is exactly the reason for the distinctly different dependence on the SOC, that we obtain in the AFM topological phase diagrams. Therefore, gap closings at $k = 0$, connected to a 1MF phase, will occur when $v_1^2 + (\sigma\Delta - d_1)^2 = \mathcal{B}^2$ depending on each σ block. Obviously the topological phase boundaries for the 1MF phase depends on the SOC strength, in *contrast* to the FM case and nanowires proposals.

On the other hand, the chiral symmetry protected points are given by $\cos(k_{\sigma,*}a) = \sigma t_1 \Delta / (t_1 d_1 - v_1 \mathcal{D}_1)$. Since $k_* \in (-\pi/2a, \pi/2a]$, we obtain $\text{sgn}[\cos(k_{\sigma,*}a)] = \text{sgn}[\sigma]$. This implies that for each σ block we obtain a single $k_{\sigma,*}$ satisfying the gap closing criterion. Even more, chiral symmetry here implies that for a point $k_{\sigma,*}$, there exists another in the $-\sigma$ spin block for $k_{-\sigma,*} = -k_{\sigma,*}$. Thus the $\pm k_*$ pair of chiral symmetry protected points found in the FM case, translates now into the $(k_{\sigma,*}, k_{-\sigma,*})$ pair of points, i.e. inversion connects the two subblocks. This also explains why we can not generally consider the quantities \mathcal{N}_σ as independent chiral symmetry related topologically invariant quantities.

Nonetheless, a direct comparison with the results presented in Fig. 10, shows that a nearest neighbor model is inadequate for capturing the physics of the exact model, since the chiral symmetry protected 2MF phase originates from $\pm k_*$ points of the same subblock. This can only occur if we take into account the next nearest neighbor contributions. In fact, for a model with *only*

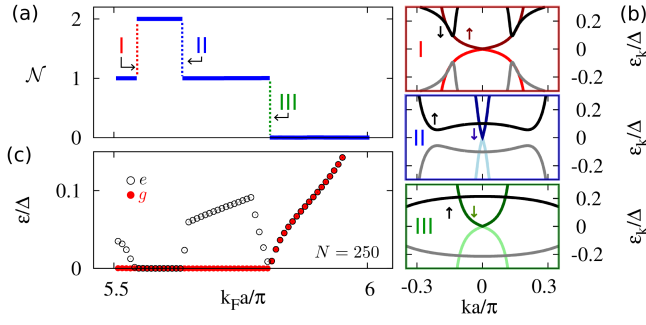


Figure 12: (a) The invariant \mathcal{N} as defined in Eq. (67) along the second green line in Fig. 9(a) for $\pi\nu_F JS = 0.85$. (b) We depict the energetically lowest dispersions corresponding to the two blocks $\sigma = \uparrow, \downarrow$ of the Hamiltonian in Eq. (63), at the transition points where $\mathcal{N} = 1 \rightarrow 2$ (I), $\mathcal{N} = 2 \rightarrow 1$ (II), and $\mathcal{N} = 1 \rightarrow 0$ (III). (c) Ground state energy (red dots) and first excited energy (black) depending on a for a chain length of $N = 250$ atoms. The calculations were performed for $\alpha = 0.03 v_F$ and $\pi\nu_F JS = 0.85$.

next nearest neighbor terms, the Hamiltonian coincides with that of Eq. (68) but with $k \rightarrow 2k$ or $a \rightarrow 2a$. Thus we may equivalently make use of Eq. (68) but now with k in the original BZ. As a result, the equation $\cos(k\sigma_* a) = \sigma t_1 \Delta / (t_1 d_1 - v_1 \mathcal{D}_1)$ can now provide a set of $\pm k_*$ points, for each σ subblock, explaining our findings.

We now proceed with a cut of the phase diagram in Fig. 9, for $\alpha = 0.03 v_F$ and $\pi\nu_F JS = 0.85$. In Fig. 12 we present: (a) the topological invariant \mathcal{N} and (b) the relevant gap closings in RBZ associated with the changes of \mathcal{N} . For the particular value of the magnetic exchange energy, the possibility of 2MF phases still appears, but has a different origin. This is clearly reflected in the fact that the topological invariant changes always by 1. This implies that only inversion-symmetric point $k = 0$ can yield gap closings. This is indeed the case, as shown in Fig. 9(b). We find that the different transitions occur due to the gap closings at the $k = 0$ for the two different $\sigma = \uparrow, \downarrow$ sub-blocks. Interestingly we observe that only after two successive gap closings at $k = 0$ for $\sigma = \uparrow$, the system becomes topologically trivial. This counter intuitive result can be naturally explained when next nearest neighbors are present, leading to a *quadratic* gap closing at $k = 0$ [66]. Essentially, the 2MF phase also in the present case, constitutes a manifestation of chiral symmetry.

In Fig. 13 we show representative MF wavefunctions for the $\mathcal{N} = 1, 2$ regions of Fig. 12. Indeed, we find the appearance of two MF when $k_F a / \pi = 5.59$. Each wavefunction is oscillating in magnitude and becomes exponentially suppressed in the bulk. As in previous sections, we denote the left and right Majorana wavefunction by $\gamma_{L/R,i}$ ($i = 1, 2$), respectively. Both γ_L and γ_R appear to be shifted spatially, with one becoming maximum at the points where the other is minimized. Furthermore, as we

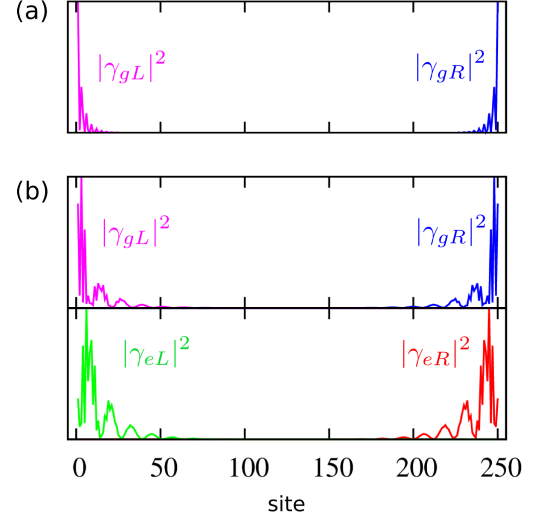


Figure 13: Majorana wavefunctions corresponding to Fig. 12 for the ground state (g) and the first excited state (e). The left and right Majorana bound states are labeled with (L) and (R) respectively. (a) The MF wavefunction in the 1MF phase shows an oscillatory dependence on the lengthscale of the adatom spacing. (b) The wavefunctions inside the 2MF phase are less localized and oscillate with smaller frequency (see Fig. 14).

show in Fig. 14, the oscillatory behavior of the wavefunctions can be attributed to the band minima of the gapped 2MF phase. Close to transition II depicted Fig. 12(a), the wavefunctions exhibit a periodicity $\cos(j\pi/2)$ which originates from the $k = 0$ point of RBZ, that coincides to the $k = \pi/2a$ point of the original BZ. In contrast, deep inside the 2MF phase and inbetween transitions I and II, the dispersion shows minima away from the $k = 0$ wavevector of the RBZ, leading to oscillations with smaller frequency (see Fig. 14).

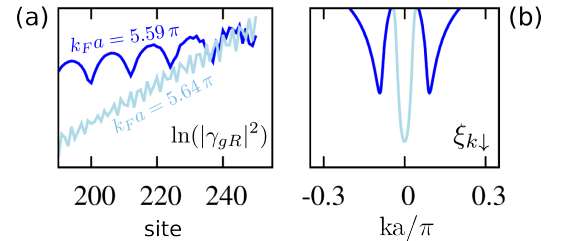


Figure 14: (a) Logarithmic plot of the right edge MF wavefunctions: **i.** deep inside the 2MF phase ($ka = 5.59\pi$) and **ii.** close to transition II ($ka = 5.64\pi$). (b) The band minimum at $k = 0$ leads to an oscillation of the MF wavefunctions on a lengthscale of the adatom spacing (see light blue curves in (a) and (b)). Band minima away from this point lead to the slow oscillatory trend (dark blue curves).

VI. CONCLUSIONS

In summary, we investigated the magnetic phase diagram and the emergence of Majorana fermions in chains of magnetic adatoms deposited on a superconducting substrate with Rashba spin-orbit coupling (SOC). By considering classical magnetic adatoms, that interact via a superexchange interaction in the additional presence of magnetic anisotropy, we identified the parameter space for which ferromagnetic (FM), antiferromagnetic (AFM) or spiral order is stabilized. The presence of magnetic anisotropy, which arise from the crystal field of the substrate, promotes the FM and AFM phases and renders them robust against thermal as also quantum fluctuations.

Motivated by recent experiments which confirmed the possibility of strong magnetic anisotropy in such type of devices, we explored the occurrence of topological superconductivity for the most prominent FM and AFM configurations. Our findings reveal a rich topological phase diagram for both cases, which can support phases of 1 or 2 MFs per edge, and can open perspectives for novel quantum computing applications. The phases with two MFs per edge are protected by chiral symmetries, which differ for each magnetic pattern. Remarkably, the topological phase diagrams for the two cases exhibit a different dependence on the strength of SOC which is directly related to the magnetic wavevector, $Q = 0$ or π . In fact, depending on the value of Q , different points of the Shiba bandstructure become topologically relevant. As a consequence, the MF wavefunctions demonstrate a variety of oscillatory characteristics which reflect the type of the underlying magnetic order.

The thorough parameter exploration performed in this work, addressing **i.** the competition of magnetic phases for the adatom chain and **ii.** the detailed topological phase diagram of the hybrid device, can motivate new experiments by employing alternative superconducting substrates or types of adatoms. In particular, the topological phase diagram can be tailored via tuning the SOC strength, the adatom spacing and the magnitude of the atomic spin. Thus the emergent interplay of magnetic and therefore topological phases in Shiba chains predicted in this work, can open the door for novel versatile and functional MF platforms.

Note added: Mind that there are two regimes which describe adatom chains on top of superconductors. We discussed the Shiba *limit* where the spectral weight lies entirely in the superconductor. If the adatoms are closely packed the adatom chain is in the metallic regime [67]. An interplay between both regimes is most likely the situation applicable to the recent experimental results of Ref. [33]. For instance, in Ref. [68] it has been shown that a shift of spectral weight to the superconducting substrate, i.e. the Shiba limit that we considered, leads to a stronger localization of Majorana wavefunctions which is in agreement with the recent observations [33].

Acknowledgements: We would like to thank G. Schön, A. Shnirman, Y. Utsumi, G. Varelogiannis, J. Wiebe, P. M. R. Brydon, A. Yazdani, S. Nadj-Perge, C. Karlewski and A. Khajetoorians for valuable discussions.

Appendix A: RKKY interaction

In this appendix we derive the effective RKKY interaction, described in Eq. (8), which is mediated by the electrons of a metallic surface with Rashba SOC. We consider a chain of magnetic adatoms arranged along the x direction. Accordingly, the Green's function that enters in Eq. (7), is given by

$$\begin{aligned} G(r\hat{x}, i\omega) &= \frac{1}{2} \sum_{\lambda=\pm} \int \frac{d\mathbf{k}}{(2\pi)^2} e^{i\mathbf{k}r \cos \varphi_{\mathbf{k}}} \frac{1}{i\omega - \xi_{k\lambda}} \\ &+ \frac{1}{2} \sum_{\lambda=\pm} \lambda \int \frac{d\mathbf{k}}{(2\pi)^2} e^{i\mathbf{k}r \cos \varphi_{\mathbf{k}}} \frac{\sin \varphi_{\mathbf{k}} \sigma_x - \cos \varphi_{\mathbf{k}} \sigma_y}{i\omega - \xi_{k\lambda}}, \\ &= \frac{1}{2} \sum_{\lambda=\pm} \int_0^\infty \frac{dk}{2\pi} \frac{k}{i\omega - \xi_{k\lambda}} [J_0(kr) - i\lambda \sigma_y J_1(kr)]. \end{aligned} \quad (\text{A1})$$

Here $J_n(kr)$ are the Bessel functions which in the limit $kr \gg 1$ can be approximated by

$$J_n(kr) \approx \sqrt{\frac{2}{\pi k|r|}} \cos\left(k|r| - \frac{n\pi}{2} - \frac{\pi}{4}\right) [\text{sgn}(r)]^n. \quad (\text{A2})$$

The remaining momentum integral in Eq. (A1) can be derived by the substitutions $k \rightarrow k_\lambda + \xi/v_F$ and $\int_0^\infty \frac{dk k}{2\pi} \rightarrow \nu_F \int_{-\infty}^\infty d\xi$, where ν_F is the density of states at the Fermi level. Within this approximation the remaining integrals in (A1) can be evaluated, and are given by the quantities

$$\begin{aligned} I_n(r, i\omega) &= \\ &\sum_{\lambda=\pm} \lambda^n \nu_F \int_{-\infty}^\infty d\xi \frac{\cos\left[(k_\lambda + \xi/v_F)|r| - \frac{n\pi}{2} - \frac{\pi}{4}\right]}{i\omega - \xi}, \end{aligned} \quad (\text{A3})$$

with $m = 0, 1$. This can be done by means of a contour integral providing

$$\frac{I_n(r, i\omega)}{i\pi\nu_F} = -\text{sgn}(\omega) \sum_{\lambda=\pm} \lambda^n e^{i\text{sgn}(\omega)(k_\lambda|r| - \frac{n\pi}{2} - \frac{\pi}{4})} e^{-\frac{|\omega r|}{v_F}}. \quad (\text{A4})$$

It follows that the electronic Green's function is approximately given by

$$G(r\hat{x}, i\omega) \approx \sqrt{\frac{1}{2\pi k_F|r|}} [I_0(r, i\omega) - i\sigma_y I_1(r, i\omega) \text{sgn}(r)]. \quad (\text{A5})$$

Note that we replaced k by k_F everywhere except for the arguments of the trigonometric functions. This approximation is valid as long as $\delta k \ll k_F$, which we assume to be the case throughout this work. In order to evaluate the susceptibility of Eq. (7), we make use of the relation

$$\begin{aligned} & \text{Tr}_\sigma \left\{ \sigma_\alpha [I_0 + i\sigma_y I_1 \text{sgn}(r)] \sigma_\beta [I_0 - i\sigma_y I_1 \text{sgn}(r)] \right\} / 2 \\ &= (I_0^2 - I_1^2) \delta_{\alpha\beta} + 2I_1^2 \delta_{\alpha,y} \delta_{\beta,y} + 2\varepsilon_{\alpha\beta y} I_0 I_1 \text{sgn}(r). \quad (\text{A6}) \end{aligned}$$

Furthermore in the limit $T \rightarrow 0$, the Matsubara sums in Eq. (7) can be converted into integrals, i.e. $T \sum_\omega \rightarrow \int_{-\infty}^{+\infty} \frac{d\omega}{2\pi}$, yielding

$$\begin{aligned} & \int_{-\infty}^{\infty} \frac{d\omega}{\pi} I_m(r, i\omega) I_n(r, i\omega) \quad (\text{A7}) \\ &= - \sum_{\lambda, \lambda' = \pm} \lambda^m (\lambda')^n \sin \left[(k_\lambda + k_{\lambda'}) |r| - \frac{n+m}{2} \pi \right] \frac{\pi v_F \nu_F^2}{|r|}, \end{aligned}$$

where $\nu_F = m/2\pi$ is the density of states for each spinband. We use Eq. (A7) together with Eq. (A6) in order to evaluate the susceptibility in Eq. (7), which yields after some algebra the well known RKKY interaction Eq. (8) for a two-dimensional metal with Rashba SOC.

-
- [1] M. Z. Hasan and C. L. Kane, Rev. Mod. Phys. **82**, 3045 (2010).
- [2] X.-L. Qi and S.-C. Zhang, Rev. Mod. Phys. **83**, 1057 (2011).
- [3] J. Alicea, Rep. Prog. Phys. **75**, 076501 (2012).
- [4] C. W. J. Beenakker, Annu. Rev. Con. Mat. Phys. **4**, 113 (2013).
- [5] P. Kotetes, New J. Phys. **15**, 105027 (2013).
- [6] L. Fu and C. L. Kane, Phys. Rev. Lett. **100**, 096407 (2008).
- [7] M. Sato, Y. Takahashi and S. Fujimoto, Phys. Rev. Lett. **103**, 020401 (2009).
- [8] J. D. Sau, R. M. Lutchyn, S. Tewari, and S. Das Sarma, Phys. Rev. Lett. **104**, 040502 (2010).
- [9] J. Alicea, Phys. Rev. B **81** 125318 (2010).
- [10] R. M. Lutchyn, J. D. Sau and S. Das Sarma, Phys. Rev. Lett. **105**, 077001 (2010).
- [11] Y. Oreg, G. Refael and F. von Oppen, Phys. Rev. Lett. **105**, 177002 (2010).
- [12] V. Mourik, K. Zuo, S. M. Frolov, S. R. Plissard, E. P. A. M. Bakkers, and L. P. Kouwenhoven, Science **336**, 1003 (2012).
- [13] M. T. Deng, C. L. Yu, G. Y. Huang, M. Larsson, P. Caroff, and H. Q. Xu, Nano Lett. **12**, 6414 (2012).
- [14] L. P. Rokhinson, Xinyu Liu, and J. K. Furdyna, Nano Lett. **8**, 795 (2012).
- [15] A. Das, Y. Ronen, Y. Most, Y. Oreg, M. Heiblum, and H. Shtrikman, Nano Lett. **8**, 887 (2012).
- [16] E. J. H. Lee, X. Jiang, R. Aguado, G. Katsaros, C. M. Lieber, and S. De Franceschi, Phys. Rev. Lett. **109**, 186802 (2012); E. J. H. Lee, X. Jiang, M. Houzet, R. Aguado, C. M. Lieber, and S. De Franceschi, Nat. Nanotechnol. **9**, 79 (2014).
- [17] A. D. K. Finck, D. J. Van Harlingen, P. K. Mohseni, K. Jung, and X. Li, Phys. Rev. Lett. **110**, 126406 (2013).
- [18] H. O. H. Churchill, V. Fatemi, K. Grove-Rasmussen, M. T. Deng, P. Caroff, H. Q. Xu, and C. M. Marcus, Phys. Rev. B **87**, 241401(R) (2013).
- [19] T.-P. Choy, J. M. Edge, A. R. Akhmerov, and C. W. J. Beenakker, Phys. Rev. B **84**, 195442 (2011).
- [20] M. Kjaergaard, K. Wölms and K. Flensberg, Phys. Rev. B **85**, 020503 (2012).
- [21] I. Martin and A. F. Morpurgo, Phys. Rev. B **85**, 144505 (2012).
- [22] S. Nadj-Perge, I. K. Drozdov, B. A. Bernevig, and A. Yazdani, Phys. Rev. B **88**, 020407(R) (2013).
- [23] S. Nakosai, Y. Tanaka, and N. Nagaosa, Phys. Rev. B **88**, 180503(R) (2013).
- [24] B. Braunecker and P. Simon, Phys. Rev. Lett. **111**, 147202 (2013).
- [25] J. Klinovaja, P. Stano, A. Yazdani, and D. Loss, Phys. Rev. Lett. **111**, 186805 (2013).
- [26] M. M. Vazifeh and M. Franz, Phys. Rev. Lett. **111**, 206802 (2013).
- [27] F. Pientka, L.I. Glazman, F. von Oppen, Phys. Rev. B **88**, 155420 (2013); Phys. Rev. B **89**, 180505(R) (2014).
- [28] Jian Li, T. Neupert, B. A. Bernevig, and A. Yazdani, arXiv:1404.4058.
- [29] K. Pöyhönen, A. Westström, J. Röntynen, T. Ojanen, Phys. Rev. B **89**, 115109 (2014); J. Röntynen, and T. Ojanen, Phys. Rev. B. **90**, 180503 (2014).
- [30] A. Heimes, P. Kotetes, and G. Schön, Phys. Rev. B **90**, 060507(R) (2014).
- [31] P. M. R. Brydon, H.-Y. Hui, and J. D. Sau, arXiv:1407.6345.
- [32] H.-Y. Hui, P. M. R. Brydon, J. D. Sau, S. Tewari, and S. Das Sarma, arXiv:1407.7519.
- [33] S. Nadj-Perge, I. K. Drozdov, J. Li, H. Chen, S. Jeon, J. Seo, A. H. MacDonald, B. A. Bernevig, and A. Yazdani, Science **346**, 602 (2014).
- [34] R. Heid, K.-P. Bohnen, I. Yu. Sklyadneva, and E. V. Chulkov, Phys. Rev. B **81**, 174527 (2010).
- [35] J. H. Dil, F. Meier, J. Lobo-Checa, L. Patthey, G. Bihlmayer, and J. Osterwalder, Phys. Rev. Lett. **101**, 266802 (2008).
- [36] K. Yaji, Y. Ohtsubo, S. Hatta, H. Okuyama, K.

- Miyamoto, T. Okuda, A. Kimura, H. Namatame, M. Taniguchi, and T. Aruga, *Nat. Comm.* **1**, 17 (2009).
- [37] B. Slomski, G. Landolt, G. Bihlmayer, J. Osterwalder, and J. H. Dil, *Scientific Reports* **3**, 1963 (2013).
- [38] G. Bihlmayer, S. Blgel, and E. V. Chulkov, *Phys. Rev. B* **75**, 195414 (2007).
- [39] M.A. Ruderman and C. Kittel, *Phys. Rev.* **96**, 99 (1954); T. Kasuya, *Prog. Theor. Phys.* **16**, 45 (1956); K. Yosida, *Phys. Rev.* **106**, 893 (1957).
- [40] I. Dzyaloshinskii, *J. Phys. Chem. Solids* **4**, 241 (1958), T. Moriya, *Phys. Rev.* **120**, 91 (1960).
- [41] Y. Kim, M. Cheng, B. Bauer, R. M. Lutchyn, S. Das Sarma, *Phys. Rev. B* **90**, 060401(R) (2014).
- [42] H. Shiba, *Prog. Theor. Phys.* **40**, 435 (1968).
- [43] S. Tewari and J. D. Sau, *Phys. Rev. Lett.* **109**, 150408 (2012).
- [44] R. Wakatsuki, M. Ezawa, Y. Tanaka, and N. Nagaosa, *Phys. Rev. B* **90**, 014505 (2014).
- [45] M. Koshino, T. Morimoto, and M. Sato, *Phys. Rev. B* **90**, 115207 (2014).
- [46] P. Kotetes, arXiv:1409.5264 (2014).
- [47] H. Imamura, P. Bruno, and Y. Utsumi, *Phys. Rev. B* **69**, 121303(R) (2004).
- [48] H. Brune and P. Gambardella, *Surface Science* **603**, 1812 (2009).
- [49] A. A. Khajetoorians, J. Wiebe, B. Chilian, S. Lounis, S. Blügel and R. Wiesendanger, *Nat. Phys.* **8**, 497 (2012).
- [50] T. Holstein and H. Primakoff, *Phys. Rev.* **58**, 1098 (1940).
- [51] A. A. Khajetoorians, B. Baxevanis, C. Hübner, T. Schlenk, S. Krause, T. O. Wehling, S. Lounis, A. Lichtenstein, D. Pfannkuche, J. Wiebe, and R. Wiesendanger, *Science* **339**, 55 (2013).
- [52] P. A. Frigeri, *Phys. Rev. Lett.* **92**, 9 (2014); P. A. Frigeri, D. F. Agterberg, and M. Sigrist, *New J. Phys.* **6**, 115 (2004).
- [53] S. Tsonis, P. Kotetes, G. Varelogiannis, and P. B. Littlewood, *J. Phys.: Condens. Matter.* **20**, 434234 (2008).
- [54] G. Varelogiannis, arXiv:1305.2976.
- [55] S. Tewari, T. D. Stanescu, J. D. Sau, S. Das Sarma, *New J. Phys.* **13**, 065004 (2011).
- [56] G. Varelogiannis, *Phys. Rev. Lett.* **85**, 4172 (2000).
- [57] A. Aperis, G. Varelogiannis, and P. B. Littlewood, *Phys. Rev. Lett.* **104**, 216403 (2010).
- [58] N. Y. Yao, L. I. Glazman, E. A. Demler, M. D. Lukin, and J. D. Sau, *Phys. Rev. Lett.* **113**, 087202 (2014).
- [59] A. V. Balatsky, I. Vekhter, and J.-X. Zhu, *Rev. Mod. Phys.* **78**, 373 (2006).
- [60] M. E. Flatte and J. M. Byers, *Phys. Rev. Lett.* **78**, 3761 (1997).
- [61] T. Mizushima, M. Sato and K. Machida, *Phys. Rev. Lett.* **109** 165301 (2012); T. Mizushima and M. Sato, *New J. of Phys.* **15**, 075010 (2013).
- [62] A. Altland and M. R. Zirnbauer, *Phys. Rev. B* **55**, 1142 (1997).
- [63] A. Kitaev *AIP Conf. Proc.*, **1134**, 22 (2009).
- [64] S. Ryu, A. Schnyder, A. Furusaki and A. Ludwig, *New J. Phys.* **12** 065010 (2010).
- [65] G. E. Volovik, “The Universe in a Helium Droplet”, Clarendon Press Oxford (2003).
- [66] K. Sun, H. Yao, E. Fradkin, and S. A. Kivelson, *Phys. Rev. Lett.* **103**, 046811 (2009).
- [67] J. Li, H. Chen, I. K. Drozdov, A. Yazdani, B. A. Bernevig, and A. H. MacDonald, *Phys. Rev. B.* **90**, 235433 (2014).
- [68] Y. Peng, F. Pientka, L. I. Glazman, and F. von Oppen, arXiv:1412.0151 (2014).